AT2019dge: a Fast-risng Type Ib Ultra-Stripped Envelope SN

Abstract

We present observations of the hydrogen-deficient optical transient AT2019dge/ZTF18abfcmjw. With a rise to maximum light of $\lesssim 3$ days over two magntiude in g and r-bands, AT2019dge is the most rapidly-rising subluminous Type I supernova (SN) discovered so far. Spectra obtained shortly after discover reveal He II flash emission, with broad He I features developed ~ 12 d after peak luminosity. to-do: more to come. AT2019dge poses chanllenge for existing models of fast-rising SNe.

Keywords: supernovae: general – supernovae: individual (AT2019dge/ZTF18abfcmjw) – surveys

1. Introduction

Type Ib/c supernovae (SNe Ib/c) are explosions of massive stars that lost their hydrogen envelopes. Their typical rise time ($t_{\rm rise} \approx 20$ d) and peak luminosity ($M_{R,\rm peak} \approx -18$ mag) suggest ejecta mass of $M_{\rm ej} \approx 2 M_\odot$ and ^{56}Ni mass of $M_{\rm Ni} \approx 0.2 M_\odot$ (Drout et al. 2011; Prentice et al. 2019). Today, a growing number of subluminous and rapidly-evolving SNe Ib/c are discovered by wide-field optical surveys, such as SN2005ek (Drout et al. 2013), SN2010X (Kasliwal et al. 2010), iPTF14gqr (De et al. 2018a), and the class of Ca-rich gap transients (Kasliwal et al. 2012). However, the physical origin of this population of SNe still remains largely elusive.

Theoretical interpretation for faint and fast SNe include scenarios not related to the explosion of massive stars (Shen et al. 2010; Sim et al. 2012; Metzger et al. 2009; Margalit & Metzger 2016), an ultra-stripped massive star progenitor (Tauris et al. 2015), core-collapse supernovae (CCSNe) with fallback (Moriya et al. 2010), and explosions of extended helium giant stars (Kleiser et al. 2018). Interaction with circumstellar material (CSM) and alternative power sources, on the other hand, are always invoked to explain more brighter and slow-evolving events (e.g. Chevalier & Irwin 2011; Hotokezaka et al. 2017).

Here we report observations of the rapidly rising ($t_{\rm rise} \lesssim 3$ d) subluminous ($M_{R,\rm peak} \approx -16$ mag) helium-rich event AT2019dge discovered by the Zwicky Transient Facility (ZTF; Bellm et al. 2019a; Graham et al. 2019), and put it in the context of ultra-stripped envelope SNe. Calculations in this paper assume a ΛCDM cosmology with $H_0 = 70$ km s^{-1} Mpc^{-1}, $\Omega_m = 0.27$ and $\Omega_\Lambda = 0.73$ (Komatsu et al. 2011). UT times are used throughout the paper. Alongside this paper, we have released our open-source analysis and all of the data utilized in this study at https://github.com/yaoyuhan/

AT2019dge. All spectra and photometry will also be made available by the WISeREP repository (Yaron & Gal-Yam 2012).

2. Observations
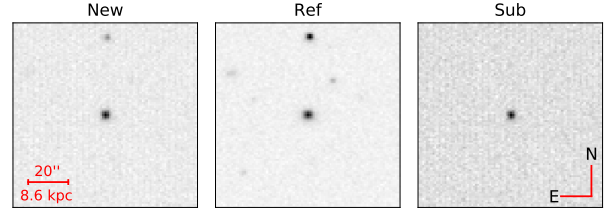
2.1. The Detection and SN Location

Figure 1. ZTF g band images centered on AT2019dge on Apr 10. From left to right are the new image, the reference image, and the subtraction image.

AT2019dge was first detected by ZTF using the Palomar Oschin Schmidt 48 inch (P48) telescope. On 2019 April 7 10:18:46 (JD = 2458580.9297), a g-band detection at 20.66 ± 0.34 mag and J2000 coordinates
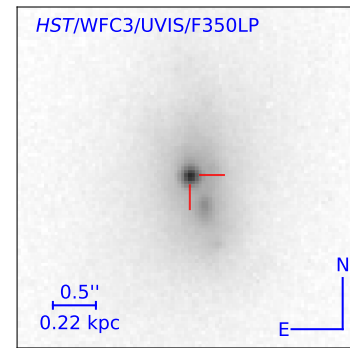

Figure 2. The position of AT2019dge (red crosshairs) in its host galaxy.
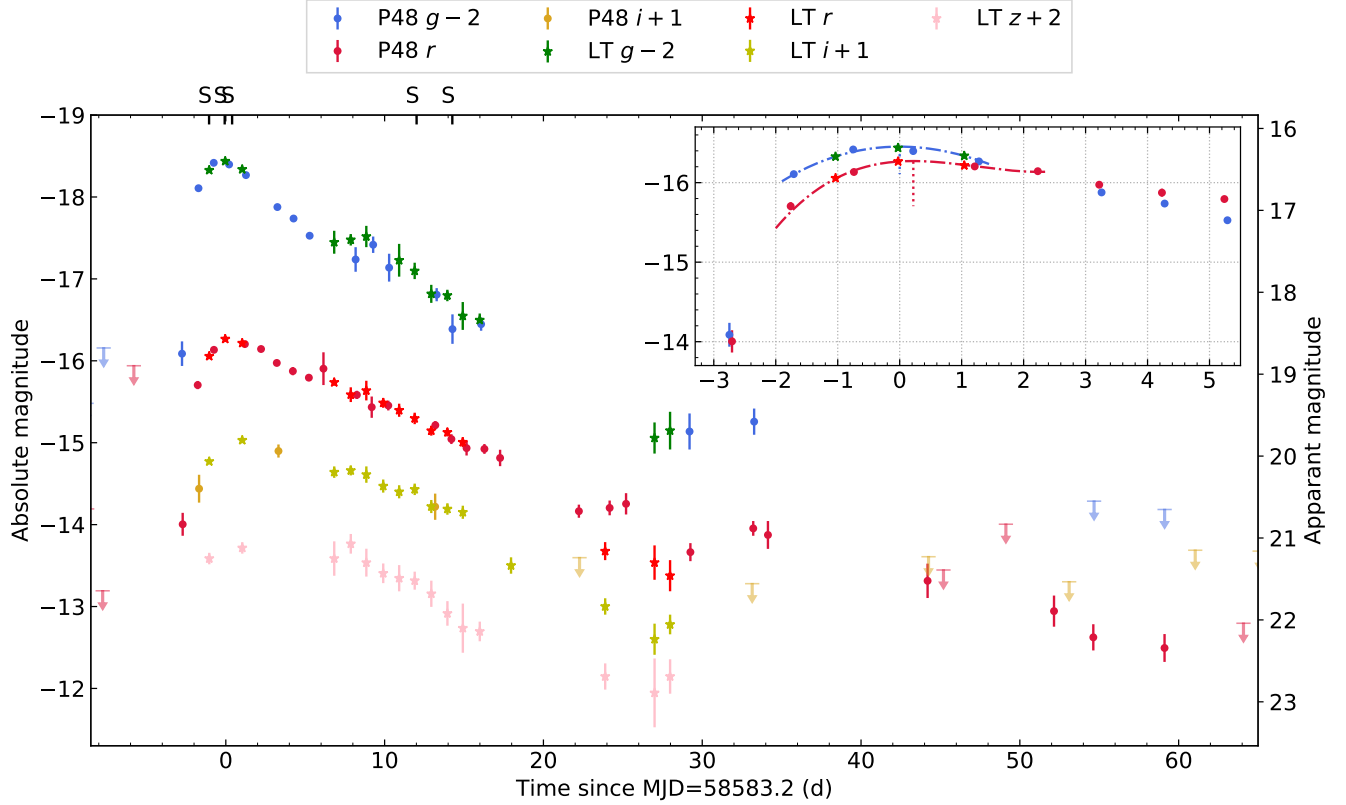
Figure 3. Galactic extinction corrected light curve of AT2019dge. The inset shows the light curve zoomed around the region of maximum light. Epochs of spectroscopy are marked with the letter 'S' along the upper axis.

$\alpha = 17^{\mathrm{h}}36^{\mathrm{m}}46.75^{\mathrm{s}}$, $\delta = +50^{\mathrm{d}}32^{\mathrm{m}}52.2^{\mathrm{s}}$ met the machine-learning thresholds (Mahabal et al. 2019) and real-time alerts were generated (Patterson et al. 2019). On April 8, the transient was flagged by a science program filter on the GROWTH Marshal (Kasliwal et al. 2019) that is designed to look for fast evolving transients. Figure 1 shows the ZTF detection image on April 10. AT2019dge resildes in a compact galaxy SDSS J173646.73+503252.3 at the redshift of $z = 0.0213$ (See Appendix B.1). Since AT2019dge is offset from the nucleus of the host in the *Hubble Space Telescope* (*HST*) image (Figure 2), the explosion can not be a tidal distruption event.

2.2. Photometry

2.2.1. Optical Photometry

We perform forced PSF photometry on ZTF difference images following the steps illustrated in Yao et al. (2019). The sky region of AT2019dge is covered by two ZTF fields with fieldid 763 and 1799. We exclude all data in field 1799 since the reference image was constructed using images obtained between May 25 2018

and July 12 2019, which is after the explosion of the transient[1].

Since field 763 was included in both the northern sky survey with two epochs (one g + one r) per three nights and the extragalactic high-cadence survey with six epochs (three g + three r) per night[2], this transient are visited muliple times every night. Therefore, single-night flux measurements in the same filter are binned (by taking the inverse variance-weighted average). This gives a pre-explosion r-band limit of 18.95 mag (5σ limit computed at the expected position of the transient) on April 4 10:36:34. Five-σ detections are converted to magnitude for further analysis.

Following the discovery of AT2019dge, we obtained follow-up photometry in $griz$ with the optical imager (IO:O) on the Liverpool Telescope (LT; Steele et al. 2004). LT and P48 photometry are shown in Figure 3. Absolute magnitude is determined by correct-

---

[1] The ZTF name (ZTF18abfcmjw) indicates that the transient was discovered in 2018. However, this is due to a candidate detection from negative subtraction (reference minus science) in 2018 in field 1799.

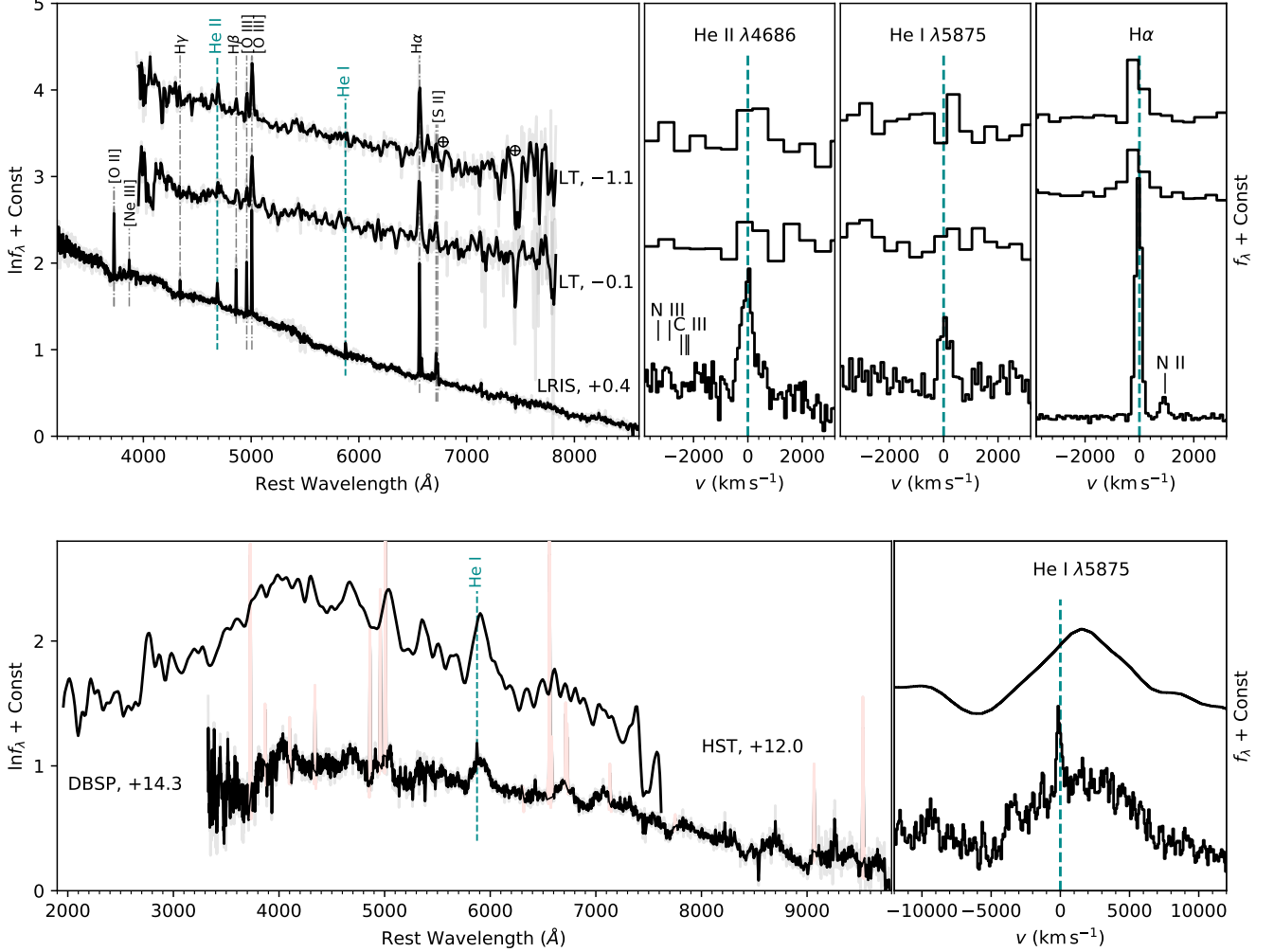[2] See Bellm et al. (2019b) for the ZTF experiments design.

Figure 4. Observed ealy-time and photosperic phase spectra of AT2019dge. For ground-based spectroscopy, the original spectra are shown in translucent colors, with the overlying black lines showing the same spectra convolved with an FWHM $= 800\,\mathrm{km\,s^{-1}}$ (for LT) or FWHM $= 200\,\mathrm{km\,s^{-1}}$ (for DBSP and LRIS) Gaussian kernel. We mask prominent galaxy lines of the DBSP spectrum in light red. In the right panels, we show spectral evolution in velocity space around prominent SN lines, where the y-axis is

ing for the distance modulus and Galactic extinction $E(B-V) = 0.022$ estimated by Schlafly & Finkbeiner (2011), which builds upon Schlegel et al. (1998). We assume $R_V = 3.1$, and adopt reddening law from Cardelli et al. (1989). We do not correct for host-galaxy contamination given the absence of Na I D absorption in all spectra at the host redshift.

We also performed forced photometry on archival PTF/iPTF difference images spanning May 07 2009 to June 13 2016[3]. No historical detections was found.

2.2.2. Swift Photometry

Space-based observations with the *Neil Gehrels Swift Observatory* (*Swift*; Gehrels et al. 2004) was triggered on April 9 and April 10. Ultraviolet/Optical Telescope (UVOT; Roming et al. 2005) data were obtained in the $UVW1$, $UVM2$, $UVW2$, U, B, and V filters.

UVOT data are reduced using HEAsoft (v6.17) with a $3''$ circular aperture. To remove host-galaxy contribution at the location of the SN, we obtained a final epoch in all broad-band filters on June 23 2019 and measured the photometry with the same aperture used for the transient. We present a table of our optical and UV photometry in Section A.1.

We note that no point sources were detected in the XRT event files with SNR > 2. The 3σ limits in count $\mathrm{s^{-1}}$ in the April 9, April 10, and June 23 observa-
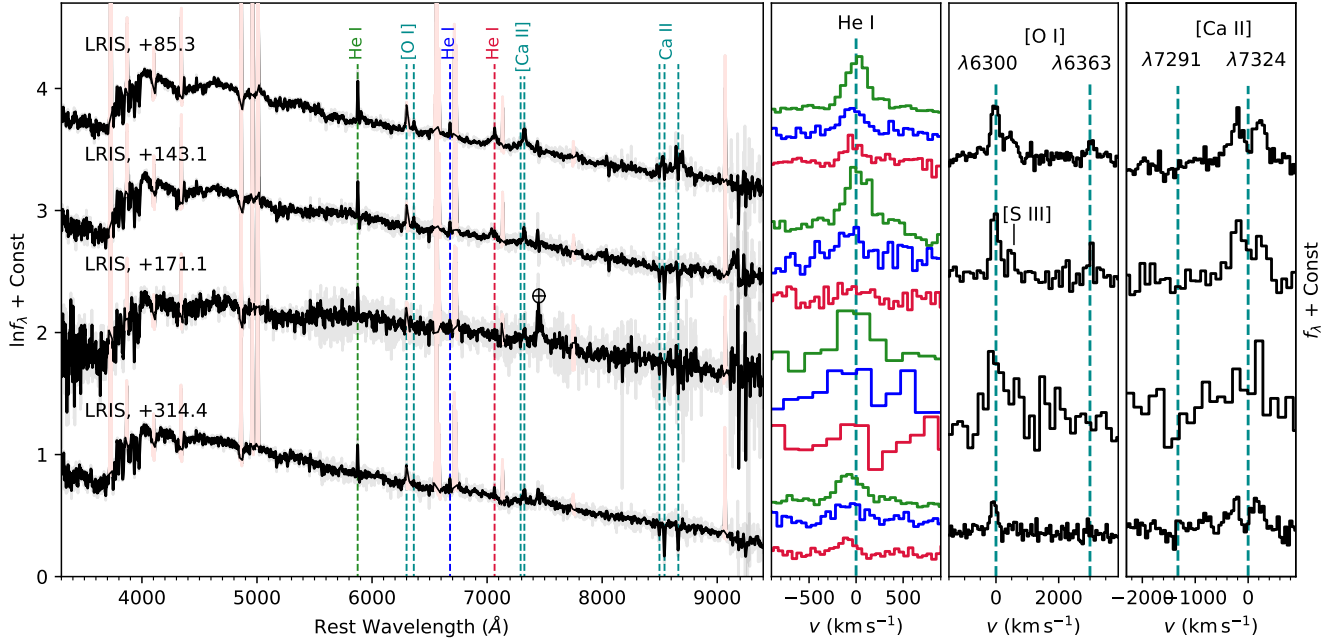
Figure 5. Observed late-time spectra of AT2019dge. See Figure 4

tions are 7.8×10^{-3}, 5.8×10^{-3}, and 6.1×10^{-3}, respectively.

2.2.3. Radio Follow-up

We observed at high frequency radio bands using the Submillimeter Array (SMA, Ho et al. 2004) on UT 2019 xx xx under its target-of-opportunity program. The project ID was xxx. Obser to-do: finish this

2.3. Spectroscopy

We obtained eight optical spectroscopic follow-up of AT2019dge from -1.1 d to $+314.4$ d relative to g-band peak using the Rapid Acquisition of Transients (SPRAT; Piascik et al. 2014) on the Liverpool Telescope (LT), the Double Spectrograph (DBSP) on the 200-inch Hale telescope (Oke & Gunn 1982), and the Low Resolution Imaging Spectrograph (LRIS) on the Keck-I telescope (Oke et al. 1995). We use the automated LT pipeline reduction and extraction for the LT spectra. The DBSP spectrum was reduced using a `PyRAF`-based reduction pipeline (Bellm & Sesar 2016). LRIS spectra were reduced and extracted using `Lpipe` (Perley 2019).

An HST slitless NUV spectrum was obtained at phase $+12.0$ d as part of our HST program (GO-15675, PI Fruchter) using the WFC3 G280 grism. We obtained a short (60 s) direct image of this field in the F300X filter to set the wavelength scale of the spectrum. We also obtained a longer exposure (200 s) in the F350LP filter (see Figure 2), which has very similar throughput to the zeroth order of the G280 grism. We convolved this

image to match the slight blurring of the zeroth order G280 grism and then scaled and subtracted it, dramatically reducing host contamination from the zeroth order host image.

A log of our spectroscopic observations is presented in Appendix B.1. We present our sequence of spectra in Figure 4 and Figure 5.

3. Properties of the Explosion and Its Host Galaxy

3.1. Light Curve Properties

3.1.1. Peak Luminosity, Rise and Decline Timescale

To estimate the epoch of maximum light, we interpolated the g- and r-band photometry with three-order polynomial functions, as is shown in the inset of Figure 3. The time range used in the fit is from MJD = 58581.2 to 58585.2. AT2019dge was found to peak at $M_{g,\mathrm{peak}} = -16.45 \pm 0.04$ mag on MJD = 58583.19, and $M_{r,\mathrm{peak}} = -16.27 \pm 0.02$ mag on MJD = 58583.39. Hereafter we use phase (Δt) to denote time with respect to the g-band maximum light epoch, MJD = 58583.2.

The g- and r-band peak luminosity of AT2019dge (≈ -16.3 mag) is around the lower limit of stripped envelope SNe, and more similar to those of the Ca-rich gap transients, which occupy the luminosity 'gap' between novae and SNe (peak absolute magnitude $M_R \approx -15.5$ to -16.5 mag).

To characterize the rise and decline timescales of AT2019dge, we calculate rise time (t_{rise}) defined by how

long it takes the r-band light curve to rise from one magnitude below peak to peak, and decline time (t_{decay}) determined by how long it takes to decline from peak by one magnitude. In Figure 6 we compare the rise time, decay time, and peak absolute magnitude between AT2019dge and other fast-evolving hydrogen-deficient transients from the literature.

It is clear from the upper panel that AT2019dge rose faster than normal Ca-rich events such as PTF09dav and PTF10iuv. The rise time of ≈ 2 d is similar to some fast evolving luminous transients (FELTs) such as KSN2015K, iPTF16asu, and SN2018gep, but its substantially low luminosity suggests that AT2019dge is physically distinct from the class of FELTs. In the subluminous regime, iPTF14gqr and iPTF16hgs have t_{rise} comparable to AT2019dge. Both transients exhibit double-peaked light curve where the first peak is postulated to be caused by the diffusion of shock-deposited energy out of an envelope around the progenitor star.

The bottom panel of Figure 6 shows that t_{decay} of AT2019dge is longer than many well-observed rapid-fading Type Ib/c SNe, such as SN2002bj, SN2018kzr, SN2005ek, and SN2019bkc. Its decay timescale is more similar to SN2010X, iPTF14gqr, as well as the population of Ca-rich transients PTF09dav, PTF10iuv, and iPTF16hgs. It has been suggested that the latter group of events have radioactivity powered main peak with low mass of nickel ($M_{Ni} \lesssim 0.1 M_\odot$).

We conclude that the AT2019dge is not one of FELTs. Its fast t_{rise} is reminiscent of shock cooling emission, and the moderate t_{decay} is consistent with coming from radioactivity.

3.1.2. Bolometric Evolution

We constructed the bolometric light curve evolution by fitting a blackbody function to the spectral energy distribution (SED). At eighteen epochs where at least detections in three filters are available, we utilized the Monte Carlo Markov Chain (MCMC) simulations with `emcee` (Foreman-Mackey et al. 2013) and adopted wide and flat prior for the blackbody radius and temperature ($0 < T_{bb} < 10^6$ K, $0 < R_{bb} < 10^6 R_\odot$). Uncertainties are estimated using the difference between the 84th and the 16th percentiles of posterior probability distributions. At five epochs that we only have photometric observations in two filters, we fit for T_{bb} and R_{bb} with no estimates on the parameter uncetainties. The SED fits are shown in Appendix A.1.

Adopting the explosion epoch estimated in Section 4.1 at $\Delta t = -3.20$ d (i.e., 0.46 d before the discovery epoch), we plot the physical evolution in Figure 7, with a comparison to peculiar SN Ic iPTF14gqr (De
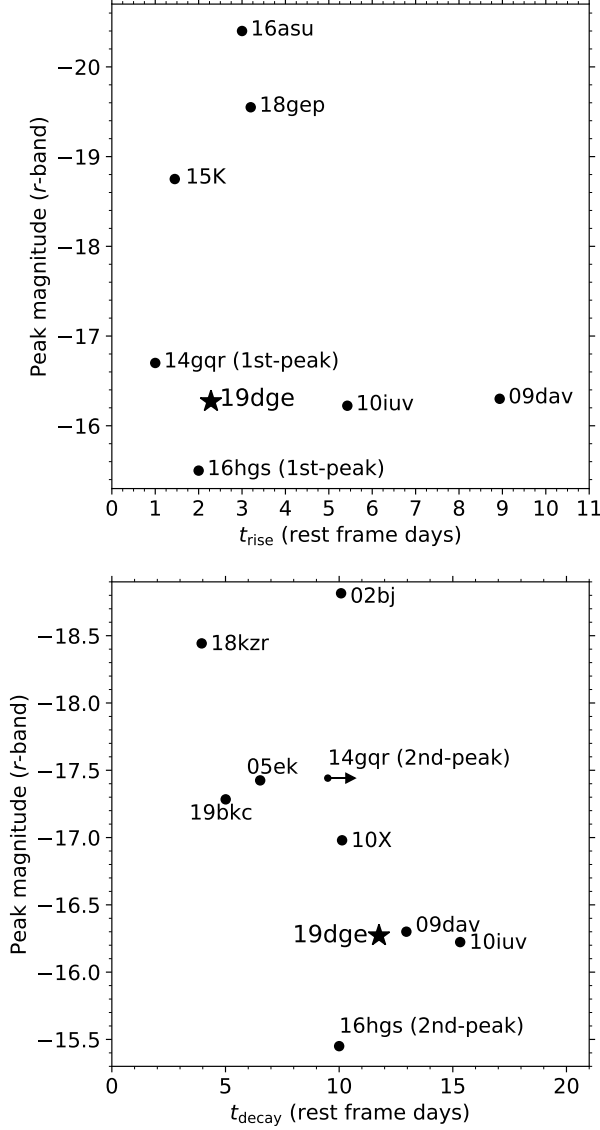
Figure 6. Comparison of the photometric evolution timescales (t_{rise} and t_{decay}) and peak absolute magnitude of AT2019dge to other H-deficient fast-evolving These include SN2002bj (Poznanski et al. 2010), SN2005ek (Drout et al. 2013), PTF09dav (Sullivan et al. 2011), SN2010X (Kasliwal et al. 2010), PTF10iuv (Kasliwal et al. 2012), iPTF14gqr (De et al. 2018a), KSN2015K (Rest et al. 2018), iPTF16asu (Whitesides et al. 2017), iPTF16hgs (De et al. 2018b), SN2018gep (Ho et al. 2019), SN2018kzr (McBrien et al. 2019), and SN2019bkc (Chen et al. 2020). For the two SNe with double peaked light curve (iPTF14gqr and iPTF16hgs), t_{rise} is estimated from model fitting to the first peak since the rise of first-peak was not observed, and t_{decay} is estimated from the decline of the second peak. Peak magnitude is given in r-band, except for KSN2015K where we only have observations in the *Kepler* white filter, and iPTF16asu where the rise was only caught in g-band (but in rest-frame r-band since this is a high-redshift event).
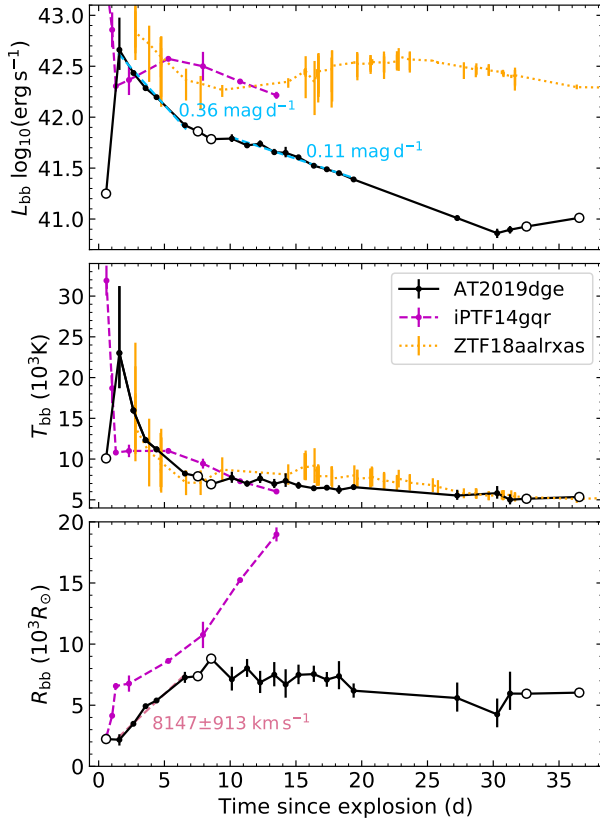
Figure 7. Evolution of blackbody properties (lumionosity, temperature, radius) over time of AT2019dge compared to iPTF14gqr and ZTF18aalrxas.

et al. 2018a) and stripped envelope SN IIb ZTF18aalrxas (Fremling et al. 2019). The bolometric luminosity peaks at $t = 1$–2 d after the assumed explosion epoch, at $\sim 5 \times 10^{42}\,\mathrm{erg\,s^{-1}}$. The initial fast drop of luminsity $(0.36\,\mathrm{mag\,d^{-1}})$ and temperature is similar to the early evolution of several stripped envelope SNe displaying double-peaked light curve, where the first peak has been modelled by cooling emission from an extended envelope around the progenitor after the core-collapse SN shock breaks out (Modjaz et al. 2019). We interpret the early evolution in the context of shock-cooling emission in Section 4.1.

The lumnosity falls at a much slower rate at later times ($t \gtrsim 9$ d) while the radius remains flat. The total integrated blackbody energy output during $t = 0.6$–30 d is $\sim 2 \times 10^{43}\,\mathrm{erg\,s^{-1}}$. Assuming that the photospheric radius linearly expands at early phase, we fit a linear function to the R_{bb} vs. Δt diagram (bottom panel of Figure 7).

3.1.3. Color Evolution

We compare the color curves of other fast transients to that of AT2019dge in Figure 8, in corresponding pairs of $B/g - R/r$ and $R/r - I/i$ colors. For double-peaked events iPTF14gqr and iPTF16hgs, "maximum" time corresponds to epoch of maximum light in the second peak.

The early-time blue color of AT2019dge arises from the high-temperature peak. Subsequently, AT2019dge has relatively typical $g - r$ color evolution among this set of transients, displaying a progression from a very blue transient ($g - r \approx -0.4$ mag) at early times to a relatively red transient ($g-r \approx 0.5$) within 10 days of explosion. This fast reddening is indicative of rapid cooling of the ejecta since the spectra at these phases are broadly consistent with featureless continua. We conclude that the multi-color light curves of the main peak of iPTF 14gqr exhibit several similarities (light curve shape and timescales) as well as unique differences (short rise time) in this sample of transients.

AT2019dge shows a color starting out blue and turning redder with time, consistent with an expanding and cooling photosphere.

Although AT2019dge has the same optical peak luminsity as Ca-rich transients, their multi-color light curves of are very different in shape. The color evolution which otherwise form a fairly homogeneous class.

to-do: AT2019dge is special in that the color even turned green a littble bit at $6 < \Delta t < 10$.

3.2. Spectroscopic Properties

3.2.1. Early Spectral Evolution

The very early spectra at -1.1, -0.1, and $+0.4$ d show a blue continuum and strong galaxy emision lines from the underlying H II region (see the top panel of Figure 4). In addition, these spectra also show prominent He I $\lambda5875$ and high-ionization He II $\lambda4686$ narrow emision lines ($\sim 600\,\mathrm{km\,s^{-1}}$). The low-velocity flash lines are not coming from the fast SN ejecta but rather from photoionized material in a region of undistrubed CSM exterior to the SN (Leonard et al. 2000). Using the line index definition given by Khazov et al. (2016), we calculated the equivalent width of He II to be -7.56 ± 1.07 -2.66 ± 1.30, and -3.77 ± 0.16 in the -1.1 d, -0.1 d, and $+0.4$ d spectra.

to-do: rewrite this: If the exploding star is embedded in circumstellar material (CSM) that is dense (n1012 cm3) and extended (r¿ 1013 cm), the CSM will be flash-ionized and quickly recombine, imprinting a strong emission-line pattern onto the underlying hot continuum. Eventually, the expanding SN ejecta plow through any nearby CSM (moving at typical expansion velocities of 104 km s1, SN ejecta cover 9×1013 cm per day)
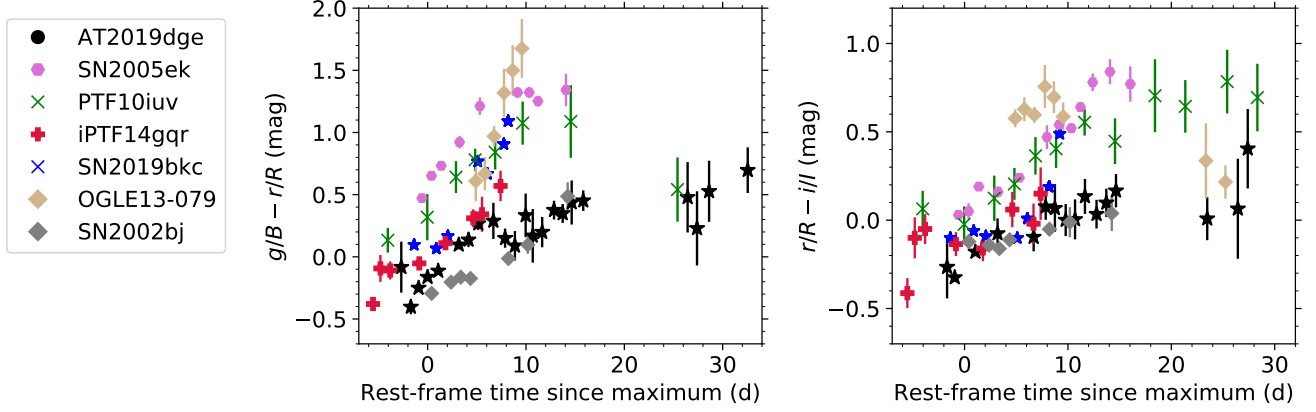
Figure 8. Comparison of the color evolution of AT2019dge with some other fast SNe shown in Figure 6. All colors have been corrected for Galactic extincton. Due to absence of photometry in identical filters, we compare colors in corresponding filter pairs of B/g, R/r and I/i.

and wipe out the emission-line spectrum, transforming it into a blue, featureless continuum that is typical for few-day old SN spectra; These lines were created by recombination of some CSM flash-ionized by a shock breakout (Khazov et al. 2016)

We make an order-of-magnitude estimate on the progenitor mass-loss rate following the xx given by Ofek et al. (2013)

3.2.2. Photosperic Phase Spectral Evolution

Broad transient features show up in the +12.0 adn +14.3 d spectra. The existence of P-Cygni He I $\lambda5876$ profile and non-existence of hydrogen is reminiscent of Type Ib SN. The HST spectrum should contain little host-galaxy contamination due to its narrow slitwidth and high resolution, otherwise we should see emission features at prominent galaxy line wavelengths (Hα, [O III], [O II], etc). The UV part is much weaker than a blackbody extrapolation opf their optical spectra would predict. This has also been seen in previous UV observations of SNe, and interpreted as strong metal-line blanketing, mostly by Fe II and Co II lines (Gal-Yam et al. 2008).

to-do: say that the undulations at 6700Å is likely just noise. Ask David to put a trace on the galaxy center and show spectrum to get a sense of the SNR

In Figure **??** we show that AT2019dge share similarity with those of normal SNe Ib/IIb in the optical region, but the spectrum does not match any known SN in 4000-4500Å and 6500–7500Å. In Figure **??** we compare the HST UV spectrum too other type of SN. AT2019dge most closely resemble SN1993J between 2000 and 4000Å. .

Enhanced (and potentially eruptive) mass-loss during the final stages of stellar evolution is a key probe

of poorly understood physics (e.g., Shiode & Quataert 2013; Smith & Arnett 2014) that sets the initial conditions to core-collapse.

We measure the velocity of the He I $\lambda5876$ line by fitting a parabola to the absorption minimum. This resulting fits give a velocity of $\approx 6000\,\mathrm{km\,s^{-1}}$ and $5900\,\mathrm{km\,s^{-1}}$ for the +12.0 d and +14.3 d spectra, respectively; At maximum light, we expect the photospheric velocity to be higher. A linear fit to the first few R_{bb} vs. time measurements (lower panel of Figure 7) gives $\approx 8150\,\mathrm{km\,s^{-1}}$. Hereafter we assume the ejecta velocity to be $v_{\mathrm{ej}} = 8150\,\mathrm{km\,s^{-1}}$

to-do: consider use Marc Williamson 2019 paper to confirm the peculiarity of this event

The UV emission fades with time from explosion as the photosphere cools and line blanketing from metals becomes important in this part of the spectrum (particularly Fe II and Fe III; see M00; DH05, DH06). Thus when reached by HST about two weeks after burst, the UV and blue optical spectrum of the supernova is dramatically altered by the metal content of the ejecta at the line forming region. In particular, the combination of both UV and optical spectra allows us to break degeneracy between temperature and metallicity.

Ba03: Baron, E., et al.2003, ApJ, 586, 1199

On the other hand, the limited number of UV spectra of Type Ib/c SNe have revealedconsiderable differences while the Type Ib SN 1983N (P03) showed several similarities toType Ia SNe in its UV spectrum, the Type Ib SN 2006jc appeared to exhibit emission linesof likely Mg II features, suggested to be associated with interaction of the SN ejecta witha pre-exisiting CSM wind. In these cases, ionization of the wind material by the SN shockwave can produce emission features of highly ionized elements (e.g. N V, N III and Si IV) aspreviously suggested
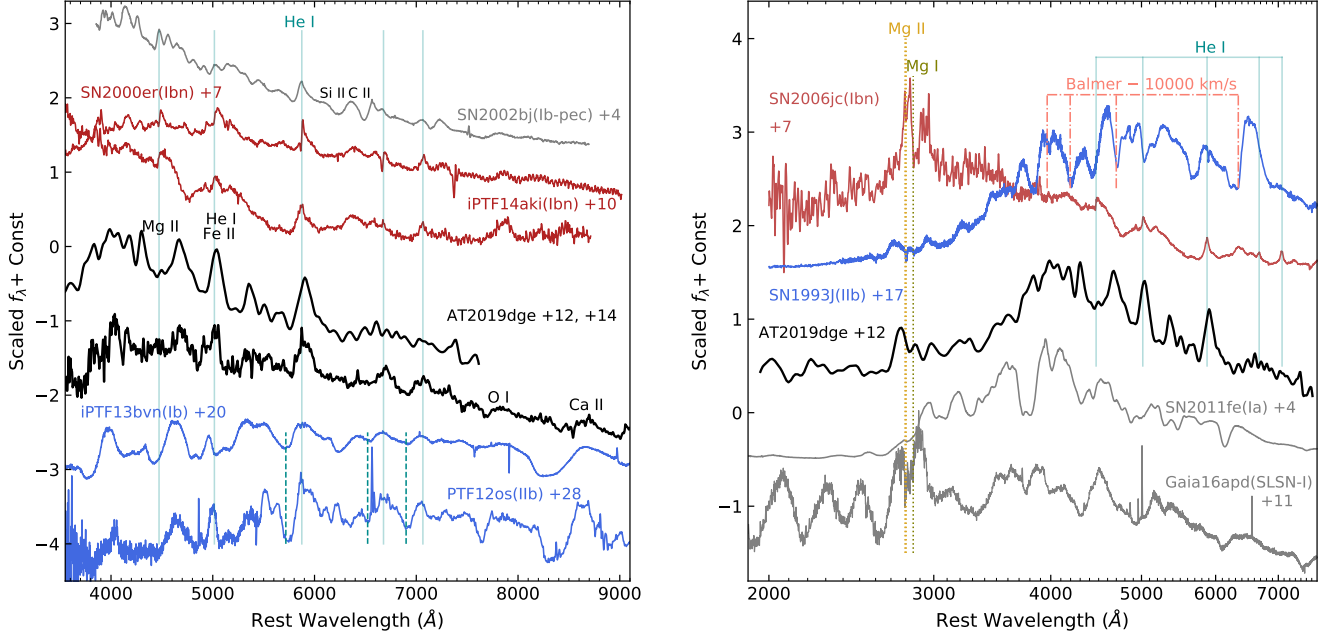
Figure 9. *Left*: AT2019dge compared with spectra of other SNe, including SN2002bj (Poznanski et al. 2010), SN2005bf (Folatelli et al. 2006), SN2008ax (Chornock et al. 2011), PTF12os and iPTF13bvn (Fremling et al. 2016) to-do: include iPTF10iuv??? iPTF16hgs???   *Right*: HST spectrum of AT2019dge compared with spectra of other SNe, including SN2006jc (Bufano et al. 2009), SN1993J (Jeffery et al. 1994), SN2011fe (Mazzali et al. 2014), and Gaia16apd (Yan et al. 2017).

in UV spectrum modeling of older events (SN 1979C and SN 1980K;Be82; Pa80; Fr84). Thus, UV spectra of core-collapse SNe are also a powerful probe of in-teraction between the SN ejecta and a pre-existing CSM around the progenitor, constrainingthe pre-explosion mass loss history of the progenitor stars

3.2.3. Late-time Spectral Evolution

In our late time spectrum obtained at +85.3, +143.1 and +171.1 d, we observe narrow emission lines that are typically the most prominent features of SNe Ib/c at nebular epochs. The emission feature at ∼ 6300Å is regularly attributed to [O I] $\lambda\lambda6300$, 6364 (**?**)

O I, Ca II and He I lines. This feature is , and (e.g., Maeda et al. 2008; Taubenberger et al. 2009). The presence or absence of this feature has often been considered the sharpest observational discrimination between core-collapse and thermonuclear SNe (e.g., Filippenko 1997). the [O i] λ λ 6300, 6364 feature consists of two similarly strong, fairly narrow emission peaks on top of a broad base (figure blah blah)

In Figure **??** we show the Its absorption minimum indicates a velocity of xxx

only three months after maximum light, a spectrum taken with LRIS The timescale to become nebular was surprising as it was faster than that of typical super-novae by a factor of a few.

3.3. Host Galaxy Properties

In Figure 2, we show the source position on the image from the Beijing-Arizona Sky Survey(BASS, Zou et al. 2017), which is part of the DESI Legacy Imaging Surveys (Dey et al. 2019). Using the xx, we calculated that AT2019dge is $0.14''$ (0.06 kpc) away from the galaxy nucleus, which is defined to be the flux-weighted first moment of the BASS g-band image.

Since there was no pre-explosion spectrum of the host galaxy, we estimated the host flux by fitting a synthetic galaxy spectrum with SDSS model magnitudes (van Velzen et al. 2019). To perform subtraction of the host flux, we calibrated the flux level in each optical spectrum against ZTF r-band photometry, interpolated to the spectroscopic epochs. We then convolved the synthetic host galaxy spectrum new Gaussian kernel to account for instrumental broadening and subtracted the broadened, synthetic spectrum from our observed spectra. A montage of the host-subtracted spectra is shown in Figure 4. The flux is normalized to the 55006000 A region in rest wavelength and offset from each other for better visualization.

In Fig we shoulw the SED of xx, which was compiled from Swfit/UVOT, SDSS, and catalogs and

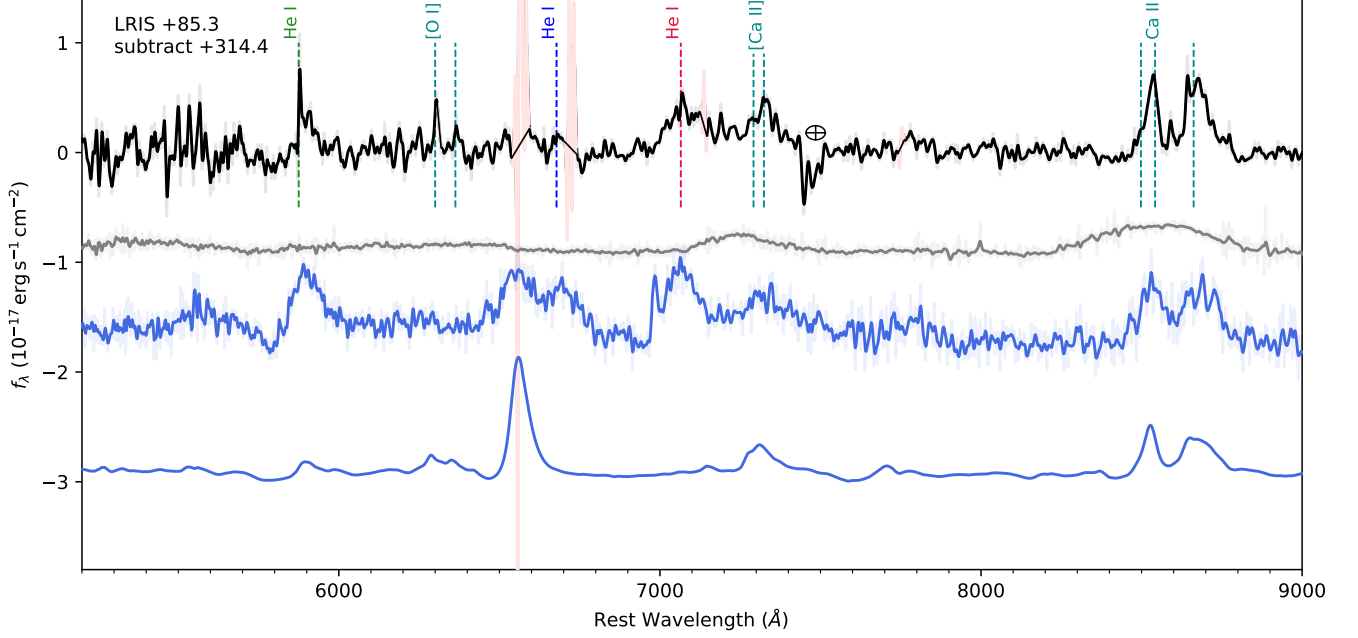We measure the metallicity of the host galaxy using the spectrum xx.

Figure 10. some caption

We infer a star-formation rate of $0.10 \pm 0.02\, M_\odot\,\mathrm{yr}^{-1}$ from the Hα emission line using the Kennicutt (1998) relation converted to use a Chabrier initial mass function (Chabrier 2003; Madau & Dickinson 2014).

We also compute the oxygen abundance using the strong-line metallicity indicator N2 (Pettini & Pagel 2004) with the updated calibration reported in Marino et al. (2013). The oxygen abundance in the N2 scale is $8.23 \pm 0.01\,\mathrm{(stat)} \pm 0.05\,\mathrm{(sys)}$.

Zhihui: We further determine the stellar mass ($M_\star$) of the host galaxy by SED modeling using CIGALE (Boquien et al. 2019). We adopt the stellar population synthesis models from Bruzual & Charlot (2003) with the Chabrier IMF (Chabrier 2003), and assume a double declining exponential star formation history (SFH). In addition, a dust component is added using the Draine & Li (2007) model to account for dust emission. Finally, the total SED model is attenuated by the Calzetti extinction curve (Calzetti et al. 2000).

The fitted SED is shown in Figure 7. The derived stellar mass is $\log M_\star/M_\odot = 8.0 \pm 0.1$, and the SFR is $0.8 \pm 0.1\, M_\odot\,\mathrm{yr}^{-1}$.

It is worth noting that while several previously reported events (SN 2005ek, SN 2010X, iPTF 14gqr) and SN 2018kzr were found in star forming host galaxies, SN 2019bkc stands out as a hostless transient offset by tens of kpc from any likely host (see Table 1).

3.4. Spectroscopy

Although there is a large diversity in the properties of these events, most of them can be grouped into events that are similar to thermonuclear SNe (e.g. PTF09dav, Sullivan et al. 2011; OGLE-2013-SN-079, Inserra et al. 2015; SN2016hnk, Galbany et al. 2019; Jacobson-Galan et al. 2019) likely arising from old white dwarfs, and those similar to Type Ib/c SNe (SN 2002bj, Poznanski et al. 2010; SN 2005ek, Drout et al. 2013; SN 2010X, Kasliwal et al. 2010; iPTF 14gqr, De et al. 2018a) possibly arising from extremely stripped massive stars or white dwarfs in close binary systems.

Ca-rich transients have detectable [O I] $\lambda\lambda\,6300$, 6364 emission in nebular spectra, but a defining feature of the class is an integrated [Ca II]/[O I] flux ratio greater than 2.

3.5. Host Environment
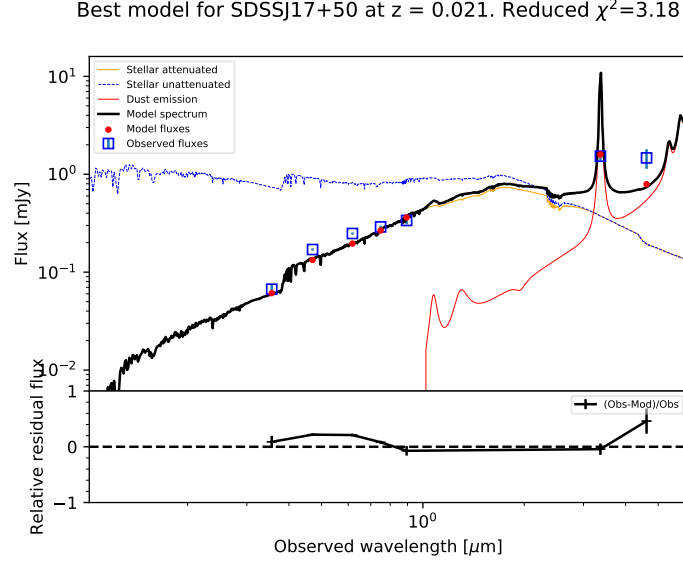
Table 1 shows a summary of our literature search.

Figure 11. Spectral energy distribution of the host galaxy of AT2019dge. The observed photometric data (with 1σ error bars) are shown in blue open squares, and the model is shown in black curve. The relative residual flux is shown in the bottom panel.

Table 1. Summary of Subluminous Fast Transient.

| Name	Redshift	Host	Offset (kpc)	Reference
SN 2002bj	0.012	NGC 1821 (small barred irregular galaxy, $D \sim 1.1$")	1.8 kpc	
SN 2005ek	0.016	UGC 2526 (edge-on spiral galaxy of morphology Sb)	30 kpc	
SN 2007ax	0.007	NGC 2577 (small lenticular galaxy with a condensed core)	1.0 kpc	
PTF 09dav	0.036	spiral galaxy	~ 40.6 kpc	
SN 2010X	0.015	NGC 1573A (small spiral galaxy, $D \sim 1.6$")	2.3 kpc	
OGLE13-079	~ 0.07	in the extreme outskirts of two ellipticals	40.2–49.9 kpc	
iPTF 14gqr	0.063	IV Zw 155 (a tidally interacting spiral galaxy)	29 kpc	De et al. (2018a)
SN 2016hnk	0.016	MCG-01-06-070 (Sb-type galaxy)	3.71	Galbany et al. (2019)
SN 2018kzr	0.053	SDSS J082853.50+010638.6 (star forming galaxy)	0.6	McBrien et al. (2019)
SN 2019bkc	~ 0.02	maybe NGC 3090 (giant elliptical in the MKW1 galaxy group)	~ 94.6	?
AT2019dge	0.021	SDSS J17+50 (small)	0.06 kpc	This work
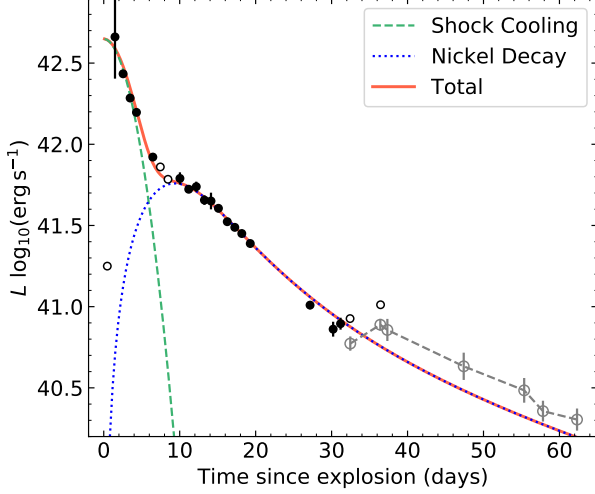
Figure 12. Bolometric light curve for AT2019dge. The quasi-bolometric light curve of AT2019dge estimated by computing νL_ν in r-band is shown as empty grey circles. The dashed green and dotted blue lines show the best fits of shock cooling and nickel decay models. The solid red line shows the combination of the two components.

4. Interpretation

4.1. Shock Cooling Powered Fast Rise

SNe light cuves are mainly powered by shock energy or radiative diffusion from a heating source. We first examine if the peak of AT2019dge is likely to be powered by the radioactive decay of ^{56}Ni $\rightarrow^{56}$ Co $\rightarrow^{56}$ Fe. With power a peak luminosity of $L_{\text{peak}} \approx 5 \times 10^{42}\,\text{erg s}^{-1}$ and a rise time of $t_{\text{peak}} \approx 2$–4 d, AT2019dge falls into the unshaded region of Kasen (2017, Fig. 1), where an unphysical condition of $M_{\text{Ni}} > M_{\text{ej}}$ is required. Therefore, we rule out radioactive decay as the power source for the fast rise of the light curve.

Next, we model the early light curve as cooling emission from shock-heated extended material, which locates at the outer layers of the progenitor or outside of the progenitor. We use models presented by Piro (2015, hereafter P15) to constrain the mass and radius of the extanded material (M_{ext} and R_{ext}, respectively), where M_{ext} includes only mass concentrated around R_{ext}. This model is built on analytical results of Nakar & Piro (2014). Details of the model fitting to multi-band observations are illustrated in Appendix A.2.

In Figure 12, bolometric light curve measured in Section 3.1 are shown in black. We also show late-time r-band νL_ν measurements in grey empty circles as a proxy of bolometric light curve evolution. The dashed green line shows the best-fit model of $M_{\text{ext}} = 9.40^{+0.35}_{-0.33} \times 10^{-2} M_\odot$, $R_{\text{ext}} = 2.69^{+0.18}_{-0.16} \times 10^{12}$ cm (i.e., $38.7^{+2.5}_{-2.4} R_\odot$),

and first light epoch at phase $t_{\text{fl}} = -3.20^{+0.03}_{-0.04}$ day (i.e., the explosion occurred 0.44 d before the first detection in g-band).

Given the simple assumptions of the model, we expect the constraints on M_{ext} and R_{ext} to be only approximatedly accurate. There are now numerous cases of early cooling envelope emission observed in CCSNe, where the extented matrial is estimated to have lower mass (~ 0.001–$0.01 M_\odot$) and larger radius ($\sim 10^{13}$ cm) compared to AT2019dge (Modjaz et al. 2019). We thus conclude that the early shock cooling emission was produced by an extended shell (instead of an envelope) with a mass of $\sim 0.1 M_\odot$ locating at a radius of $\sim 3 \times 10^{12}$ cm.

to-do: try to see if puffier helium star produce lower ejecta mass

Table 2. shock P15.

Name	Type	R_{ext} (10^{12} cm)	M_{ext} ($10^{-2} M_\odot$)
iPTF16hgs	Ca-rich	0.9	8
AT2019dge	Ib-pec	$2.69^{+0.34}_{-0.16}$	$9.40^{+0.69}_{-0.33}$
iPTF14gqr	Ic-pec	30^{+3}_{-3}	$0.88^{+0.08}_{-0.07}$
iPTF15dtg	Ic	83	5
SN2016gkg	IIb	$4.00^{+0.05}_{-0.05}$	$2.50^{+0.01}_{-0.01}$
ZTF18aalrxas	IIb	73^{+3}_{-2}	$4.3^{+0.14}_{-0.13}$

NOTE—Reference: iPTF14gqr (De et al. 2018a), SN2016gkg (Arcavi et al. 2017), ZTF18aalrxas (Fremling et al. 2019)

4.2. Radioactivity Powered Main Peak

After subtracting the shock cooling emission from the bolometric light curve, the remaining light curve has a peak luminosity of $L_{\text{peak}} \approx 6 \times 10^{41}\,\text{erg s}^{-1}$ and a rise time of $t_{\text{peak}} \approx 9$ d. In the shaded region of Kasen (2017, Fig. 1), this falls into the $M_{\text{Ni}} = 0.1 M_{\text{ej}}$ and $M_{\text{Ni}} = 0.01 M_{\text{ej}}$ lines, indicating that the remaining component can be powered by ^{56}Ni decay. Here we use two methods to estimate M_{ej} and M_{Ni}.

First of all, we use analytical models (Arnett 1982; Valenti et al. 2008; Wheeler et al. 2015) to constrain the nickel mass (M_{Ni}), a characteristic photon diffusion timescale (τ_{m}), and a characteristic γ-ray escape timescale (t_0). Details of the model fitting are illustrated in Appendix A.3. The dotted blue line in Figure 12 shows the best-fit model of $M_{\text{Ni}} = 1.69^{+0.05}_{-0.04} \times 10^{-2} M_\odot$, $\tau_{\text{m}} = 7.15 \pm 0.16$ d, and $t_0 = 22.17^{+0.74}_{-0.73}$ d. Thus, using Equation (A5), the ejecta mass can be estimated to be

$$M_{\text{ej}} = (0.46 \pm 0.02) M_\odot \frac{v_{\text{ej}}}{8150\,\text{km s}^{-1}} \frac{0.07\,\text{cm}^2\,\text{g}^{-1}}{\kappa_{\text{opt}}}$$

Recently, Khatami & Kasen (2019, hereafter KK19) presents improved analytic relations (compared with the

original Arnett 1982 model) between t_{peak} and L_{peak}. When $t < 10$ d, $\varepsilon_{\mathrm{Ni}}(t) \gg \varepsilon_{\mathrm{Co}}(t)$ (see Equations A2, A3), and thus we have an exponential heating function

$$L_{\mathrm{heat}}(t) = L_0 e^{-t/\tau_{\mathrm{Ni}}} \qquad (1)$$

where $L_0 = M_{\mathrm{Ni}} \times \epsilon_{\mathrm{Ni}}$. In this case, KK19 (Eq. 21) shows that the relation between peak time and luminosity is:

$$L_{\mathrm{peak}} = \frac{2L_0\tau_{\mathrm{Ni}}^2}{\beta^2 t_{\mathrm{peak}}^2}\left[1 - (1 + \beta t_{\mathrm{peak}}/\tau_{\mathrm{Ni}})e^{-\beta t_{\mathrm{peak}}/\tau_{\mathrm{Ni}}}\right] \quad (2)$$

where $\beta \sim 4/3$ gives a reasonable match to numerical simulations. With $L_{\mathrm{peak}} \approx 6 \times 10^{41}\,\mathrm{erg\,s^{-1}}$ and $t_{\mathrm{peak}} \approx 9$ d, we get an estimate of $M_{\mathrm{Ni}} \sim 0.018 M_\odot$.

M_{ej} can be estimated using Eq. 23 of KK19:

$$\frac{t_{\mathrm{peak}}}{t_{\mathrm{d}}} = 0.11 \ln\left(1 + \frac{9\tau_{\mathrm{Ni}}}{t_{\mathrm{d}}}\right) + 0.36, \qquad (3)$$

where t_{d} is the characteristic timescale without any numerical factors

$$t_{\mathrm{d}} = \left(\frac{\kappa_{\mathrm{opt}} M_{\mathrm{ej}}}{v_{\mathrm{ej}} c}\right)^{1/2}. \qquad (4)$$

We derive $t_{\mathrm{d}} \approx 16.2$ d, which implies

$$M_{\mathrm{ej}} \approx 0.30 M_\odot \frac{v_{\mathrm{ej}}}{8150\,\mathrm{km\,s^{-1}}} \frac{0.07\,\mathrm{cm^2\,g^{-1}}}{\kappa_{\mathrm{opt}}}$$

In conclusion, the estimates derived from simplified modelling fitting and new analytic relations from KK19 are roughly the same. Ejecta mass and nickle mass from the explosion of AT2019dge are very small, $M_{\mathrm{ej}} \sim 0.3 M_\odot$, $M_{\mathrm{Ni}} \sim 0.02 M_\odot$.

4.3. A Highly Stripped Progenitor in a Binary System

The shock cooling powered early emission followed by the radioactivity powered decay indicates that AT2019dge is associated with the class of iron core-collapse events. The small amout of ejecta mass requires extreme stripping prior to the explosion, and rules out single massive star to be the progenitor. The helium-rich photosperic phase spectra suggests that the bulk of the ejecta should be helium.

The evolution of binary massive stars

Tight helium star–NS binary systems, presumably created in the common-envelope phase from high-mass X-ray binaries, can lead to the extrame stripping of the helium envelope pand result in SNe with ejecta masses of the order of 0.1Msun

Many progenitors are expected to have a helium mass above the critical helium mass (0.1 Msun, Hachingerr 2012) required to observe optical helium features Tauris 2015 and thus may be observed as SN Ib like AT2019dge.

In this picture, the helium-star mass transfer rate is 3–4 orders of magnitude greater than the Eddington accretion rate for NSs and $> 99.9\%$ of the transferred mass is lost from the system (Tauris et al. 2015), forming a shell of $\sim 0.1 M_\odot$ and 3×10^{12} cm at the time of explosion.

to-do: This is actually not ultra-stripped SN: Mej larger than 0.2 Msun. Can form this using HMLB – Case BB RLO – stripp – double NS. OR. Massive star explosion??

5. Discussion

Woosley (2019) shows that mass-losing helium stars with initial masses between 2.5–3.2 $M_\odot$ experience raidus expansion after helium depletion (but lack a strong silicon flash), which gives rise to the early-time shock cooling emission out of the ejected helium envelope. If the explosion makes substantial ^{56}Ni, then the light curve may have two peaks, the second resembling a SN Ib but occurring earlier due to the low M_{ej}.

massive mass-loss episode that takes place just prior to the explosion (Shiode & Quataert 2014)

Progenitor: why so rare??? Could the progenitor be a helium rich WR star, perhaps recently transitioned from an LBV phase

Constraints on event rate?

6. Conclusion

In this paper we have presented observations and modeling of the fast transient AT2019dge. We summarize our primary observational findings below:

- Peak absolute magnitude of MB = dd mag and decline parameter of hah mag.

- Total Nickel and ejecta masses of $M_{\mathrm{Ni}} = 0.03 \pm 0.01$ and $Mej = 0.9 \pm 0.3 M_\odot$, respectively.

The combination of depth, cadence and sky coverage offered by ongoing time domain surveys enables detection within one day of the explosion, opening a new window into the relatively unexplored early phase of these events.

Enhanced (and potentially eruptive) mass-loss during the final stages of stellar evolution is a key probe of poorly understood physics (e.g., Shiode & Quataert 2013; Smith & Arnett 2014) that sets the initial conditions to core-collapse.

Despite the steady increase in the number of events in the class of sub-luminous transients, the total number of well-studied events remain still small (≈ 10). An all-sky two-day cadence survey with ZTF Phase II is ideally positioned to probe this rare population over a sufficiently large volume (given the deeper limiting magnitude of

ZTF compared to other ongoing time domain surveys) to address questions regarding their intrinsic properties such as luminosity functions, spectroscopic diversity and ejecta mass distributions of the different sub-types and their volumetric rates. As likely tracers of the end points of white dwarfs and massive stars in extreme binary systems, their intrinsic rates are not only important from the point of view of understanding these rare transient phenomena but also have direct implications for current and future experiments in the field of gravitational wave astronomy. With a higher cadence than the nominal 3-day public survey in Phase I, the 2-day cadence in g and r bands will be particularly sensitive to the population of fastest transients in the local universe, of which only a handful are known, while the two-color coverage will also be a powerful diagnostic of the intrinsic color of these events.

Appendix A   UV and Optical Photometry

A.1 Data

Table 3. Optical and UV photometry for AT2019dge.

Date (JD)	Instrument	Filter	m	σ_m
58582.1544	LT+IOO	g	18.59	0.01
58582.1552	LT+IOO	r	18.84	0.02
58582.1575	LT+IOO	i	19.11	0.02
58582.1583	LT+IOO	z	19.28	0.07
58583.1637	LT+IOO	g	18.48	0.02
58583.1645	LT+IOO	r	18.63	0.01
58584.2324	LT+IOO	g	18.58	0.01
58584.2332	LT+IOO	r	18.68	0.02
58584.2355	LT+IOO	i	18.85	0.02
58584.2363	LT+IOO	z	19.15	0.07
58590.0252	LT+IOO	g	19.47	0.14
58590.0260	LT+IOO	r	19.16	0.04
58590.0268	LT+IOO	i	19.24	0.07
58590.0277	LT+IOO	z	19.28	0.21
58591.0676	LT+IOO	g	19.44	0.07
58591.0685	LT+IOO	r	19.31	0.09
58591.0693	LT+IOO	i	19.22	0.06
58591.0701	LT+IOO	z	19.10	0.12
58592.0472	LT+IOO	g	19.40	0.13
58592.0472	LT+IOO	r	19.26	0.12
58592.0489	LT+IOO	i	19.27	0.10
58592.0497	LT+IOO	z	19.33	0.17
58593.1109	LT+IOO	r	19.41	0.06
58593.1117	LT+IOO	i	19.41	0.08
58593.1125	LT+IOO	z	19.46	0.12
58594.1142	LT+IOO	g	19.69	0.20
58594.1150	LT+IOO	r	19.50	0.08
58594.1158	LT+IOO	i	19.48	0.08
58594.1167	LT+IOO	z	19.52	0.16
58595.0926	LT+IOO	g	19.82	0.10
58595.0935	LT+IOO	r	19.60	0.07
58595.0943	LT+IOO	i	19.45	0.07
58595.0951	LT+IOO	z	19.55	0.11
58596.1380	LT+IOO	g	20.10	0.11
58596.1388	LT+IOO	r	19.75	0.06
58596.1396	LT+IOO	i	19.66	0.08
58596.1405	LT+IOO	z	19.71	0.16
58597.1508	LT+IOO	g	20.12	0.07
58597.1516	LT+IOO	r	19.77	0.05
58597.1539	LT+IOO	i	19.69	0.07
58597.1547	LT+IOO	z	19.95	0.15
58598.1207	LT+IOO	g	20.37	0.17
58598.1218	LT+IOO	r	19.89	0.06
58598.1247	LT+IOO	i	19.73	0.08
58598.1257	LT+IOO	z	20.13	0.30
58599.1894	LT+IOO	g	20.42	0.08

Table 3 *continued*

Table 3 *(continued)*

Date (JD)	Instrument	Filter	m	σ_m
58599.1918	LT+IOO	z	20.17	0.12
58601.1606	LT+IOO	i	20.38	0.10
58607.0861	LT+IOO	r	21.22	0.11
58607.0890	LT+IOO	i	20.88	0.10
58607.0900	LT+IOO	z	20.72	0.16
58610.1965	LT+IOO	g	21.86	0.19
58610.1974	LT+IOO	r	21.36	0.21
58610.1982	LT+IOO	i	21.28	0.19
58610.1990	LT+IOO	z	20.92	0.42
58611.1743	LT+IOO	g	21.77	0.23
58611.1751	LT+IOO	r	21.52	0.19
58611.1759	LT+IOO	i	21.10	0.12
58611.1767	LT+IOO	z	20.72	0.21
58580.4421	P48+ZTF	g	20.83	0.15
58581.4807	P48+ZTF	g	18.81	0.03
58582.4396	P48+ZTF	g	18.50	0.02
58583.4082	P48+ZTF	g	18.52	0.04
58584.4691	P48+ZTF	g	18.65	0.02
58586.4480	P48+ZTF	g	19.04	0.02
58587.4658	P48+ZTF	g	19.18	0.03
58588.4794	P48+ZTF	g	19.39	0.04
58591.3740	P48+ZTF	g	19.68	0.15
58592.4784	P48+ZTF	g	19.50	0.10
58593.4841	P48+ZTF	g	19.78	0.17
58596.4781	P48+ZTF	g	20.11	0.08
58597.4728	P48+ZTF	g	20.53	0.18
58599.2766	P48+ZTF	g	20.47	0.08
58612.4016	P48+ZTF	g	21.78	0.22
58616.4688	P48+ZTF	g	21.66	0.16
58580.4842	P48+ZTF	r	20.89	0.14
58581.4308	P48+ZTF	r	19.19	0.05
58582.4516	P48+ZTF	r	18.76	0.02
58584.4009	P48+ZTF	r	18.69	0.02
58585.4191	P48+ZTF	r	18.75	0.03
58586.4101	P48+ZTF	r	18.92	0.03
58587.4222	P48+ZTF	r	19.02	0.05
58588.4300	P48+ZTF	r	19.10	0.03
58589.3489	P48+ZTF	r	18.99	0.20
58591.4525	P48+ZTF	r	19.31	0.05
58592.3880	P48+ZTF	r	19.46	0.13
58593.4315	P48+ZTF	r	19.44	0.06
58596.3929	P48+ZTF	r	19.68	0.05
58597.4050	P48+ZTF	r	19.85	0.06
58598.3610	P48+ZTF	r	19.96	0.09
58599.4846	P48+ZTF	r	19.97	0.06
58600.4715	P48+ZTF	r	20.08	0.10
58605.4333	P48+ZTF	r	20.73	0.08
58607.3705	P48+ZTF	r	20.69	0.09
58608.4033	P48+ZTF	r	20.64	0.13
58612.4549	P48+ZTF	r	21.23	0.11
58616.4117	P48+ZTF	r	20.94	0.09
58617.3380	P48+ZTF	r	21.02	0.17
58627.3911	P48+ZTF	r	21.58	0.21
58635.3518	P48+ZTF	r	21.95	0.19

Table 3 *continued*

Table 3 *(continued)*

Date (JD)	Instrument	Filter	m	σ_m
58581.5163	P48+ZTF	i	19.44	0.17
58586.5159	P48+ZTF	i	18.98	0.08
58596.3822	P48+ZTF	i	19.66	0.16
58637.8263	P48+ZTF	r	22.27	0.16
58642.3119	P48+ZTF	r	22.40	0.17
58582.8289	$Swift$+UVOT	B	18.68	0.40
58582.8280	$Swift$+UVOT	U	18.80	0.10
58582.8346	$Swift$+UVOT	$UVM2$	18.55	0.07
58582.8261	$Swift$+UVOT	$UVW1$	18.61	0.19
58582.8299	$Swift$+UVOT	$UVW2$	18.68	0.11
58582.8337	$Swift$+UVOT	V	18.29	0.11
58583.5775	$Swift$+UVOT	B	18.46	0.29
58583.5766	$Swift$+UVOT	U	19.22	0.10
58583.5833	$Swift$+UVOT	$UVM2$	18.85	0.09
58583.5747	$Swift$+UVOT	$UVW1$	18.49	0.14
58583.5785	$Swift$+UVOT	$UVW2$	18.87	0.10
58583.5823	$Swift$+UVOT	V	18.51	0.11

NOTE—m and σ_m are observed magnitude (without extinction correction) in AB system.

The full set of photometry is listed in Table 3.

In Figure A1 we show the photometry interpolated onto common epochs, and fit to a blackbody function to derive the photospheric evolution (see Section 3.1). The resulting evolution in bolometric lumonosity, photospheric radius, and effective temperatures is listed in Table 4

A.2 Modelling Early Light Curve

To model the early light curve with the P15 model, we fix $\kappa \sim 0.2\,\mathrm{cm^2\,g^{-1}}$ as appropriate for a hydrogen-deficient ionized gas, and assign wide flat priors for all model parameters, as summarized in Table 5. We only include observations up to $\Delta t = 2\,\mathrm{d}$ in the fitting. We found that this particular choice of Δt — 2 d instead of 1 d or 3 d — in general does not affect the final inference for the model parameters. Figure A2 shows the corner plot of $\lg R_{\mathrm{ext}}$, $\lg M_{\mathrm{ext}}$, and t_{fl}. For clarity, E_{51} and M_{core} are excluded as they do not exhibit strong covariance with the parameters shown here. These two parameters are highly anti-correlated with each other over a wide range of their priors. We find $E_{51} \propto M_{\mathrm{core}}^{0.7}$, as implied by Piro (2015, Eq 3). The amount of energy passed into the extended material is well constrained to be $E_{\mathrm{ext}} = (1.15 \pm 0.07) \times 10^{50}\,\mathrm{erg\,s^{-1}}$.

The maximum a posteriori model is visualized by solid lines in Figure A3 color-coded in different filters. Note that the fitting is not perfect at the UV bands since the SED is not exactly a blackbody at peak (see Figure A1). The rising part of the model does not closely match to data due to the ignorance of the density structure of the

Table 4. Physical evolution of AT2019dge from blackbody fits.

Δt	$L(10^{41}\,\mathrm{erg\,s^{-1}})$	$R\ (10^3\,R_\odot)$	$T\ (10^3\,\mathrm{K})$
-2.74	1.78	2.23	10.08
-1.72	$45.83^{+49.11}_{-16.74}$	$2.18^{+0.45}_{-0.48}$	$23.01^{+8.21}_{-4.31}$
-0.66	$27.17^{+1.13}_{-1.08}$	$3.48^{+0.08}_{-0.08}$	$15.97^{+0.34}_{-0.33}$
0.27	$19.26^{+0.76}_{-0.73}$	$4.92^{+0.14}_{-0.14}$	$12.32^{+0.29}_{-0.29}$
1.10	$15.72^{+0.46}_{-0.42}$	$5.39^{+0.14}_{-0.14}$	$11.20^{+0.23}_{-0.22}$
3.26	$8.34^{+0.22}_{-0.20}$	$7.27^{+0.46}_{-0.44}$	$8.22^{+0.31}_{-0.28}$
4.24	7.25	7.37	7.89
5.25	6.09	8.81	6.90
6.83	$6.16^{+0.63}_{-0.45}$	$7.12^{+1.02}_{-0.92}$	$7.70^{+0.74}_{-0.62}$
7.98	$5.28^{+0.23}_{-0.21}$	$8.02^{+0.76}_{-0.70}$	$6.98^{+0.39}_{-0.35}$
8.98	$5.48^{+0.43}_{-0.35}$	$6.86^{+0.95}_{-0.87}$	$7.61^{+0.65}_{-0.55}$
10.05	$4.53^{+0.35}_{-0.26}$	$7.49^{+1.04}_{-0.95}$	$6.95^{+0.61}_{-0.51}$
10.92	$4.47^{+0.64}_{-0.44}$	$6.70^{+1.24}_{-1.09}$	$7.32^{+0.93}_{-0.74}$
11.89	$4.03^{+0.24}_{-0.21}$	$7.49^{+0.83}_{-0.76}$	$6.75^{+0.45}_{-0.40}$
13.06	$3.34^{+0.10}_{-0.10}$	$7.55^{+0.69}_{-0.64}$	$6.42^{+0.31}_{-0.29}$
14.05	$3.08^{+0.10}_{-0.09}$	$7.09^{+0.63}_{-0.58}$	$6.49^{+0.31}_{-0.28}$
14.97	$2.82^{+0.14}_{-0.12}$	$7.38^{+1.23}_{-1.07}$	$6.21^{+0.57}_{-0.48}$
16.09	$2.45^{+0.09}_{-0.09}$	$6.19^{+0.59}_{-0.57}$	$6.56^{+0.33}_{-0.29}$
23.96	$1.02^{+0.06}_{-0.06}$	$5.59^{+1.27}_{-1.11}$	$5.53^{+0.70}_{-0.53}$
27.00	$0.73^{+0.08}_{-0.06}$	$4.25^{+1.30}_{-1.06}$	$5.81^{+0.88}_{-0.68}$
27.98	$0.79^{+0.07}_{-0.06}$	$5.95^{+1.79}_{-1.34}$	$5.01^{+0.66}_{-0.57}$
29.23	0.84	5.94	5.13
33.24	1.03	6.03	5.35

Table 5. Shock cooling model parameters θ and their priors

θ	Description	Prior
$\lg R_{\mathrm{ext}}$	$\log_{10}$ of extented material radius in cm	$\mathcal{U}(-5, 25)$
$\lg M_{\mathrm{ext}}$	$\log_{10}$ of extented material mass in $M_\odot$	$\mathcal{U}(-4, 0)$
t_{fl}	first light epoch in MJD relative to 58583.2	$\mathcal{U}(-8, -2.76)$
E_{51}	SN energy divided by $10^{51}\,\mathrm{erg\,s^{-1}}$	$\mathcal{U}(0.01, 10)$
M_{core}	core mass in $M_\odot$	$\mathcal{U}(0.1, 100)$

stellar profile. Nevertheless, the peak of the light curve is well captured by this model.

A.3 Modelling the Main Peak

For $^{56}\mathrm{Ni} \rightarrow\ ^{56}\mathrm{Co} \rightarrow\ ^{56}\mathrm{Fe}$ decay powered explosions, the energy deposition rate is

$$\varepsilon_{\mathrm{rad}} = \varepsilon_{\mathrm{Ni},\gamma}(t) + \varepsilon_{\mathrm{Co},\gamma}(t) \tag{A1}$$

$$\varepsilon_{\mathrm{Ni},\gamma}(t) = \epsilon_{\mathrm{Ni}} e^{-t/\tau_{\mathrm{Ni}}} \tag{A2}$$

$$\varepsilon_{\mathrm{Co},\gamma}(t) = \epsilon_{\mathrm{Co}} \left(e^{-t/\tau_{\mathrm{Co}}} - e^{-t/\tau_{\mathrm{Ni}}} \right) \tag{A3}$$

where $\epsilon_{\mathrm{Ni}} = 3.90 \times 10^{10}\,\mathrm{erg\,g^{-1}\,s^{-1}}$, $\epsilon_{\mathrm{Co}} = 6.78 \times 10^9\,\mathrm{erg\,g^{-1}\,s^{-1}}$, $\tau_{\mathrm{Ni}} = 8.8\,\mathrm{d}$ and $\tau_{\mathrm{Co}} = 111.3\,\mathrm{d}$ are the
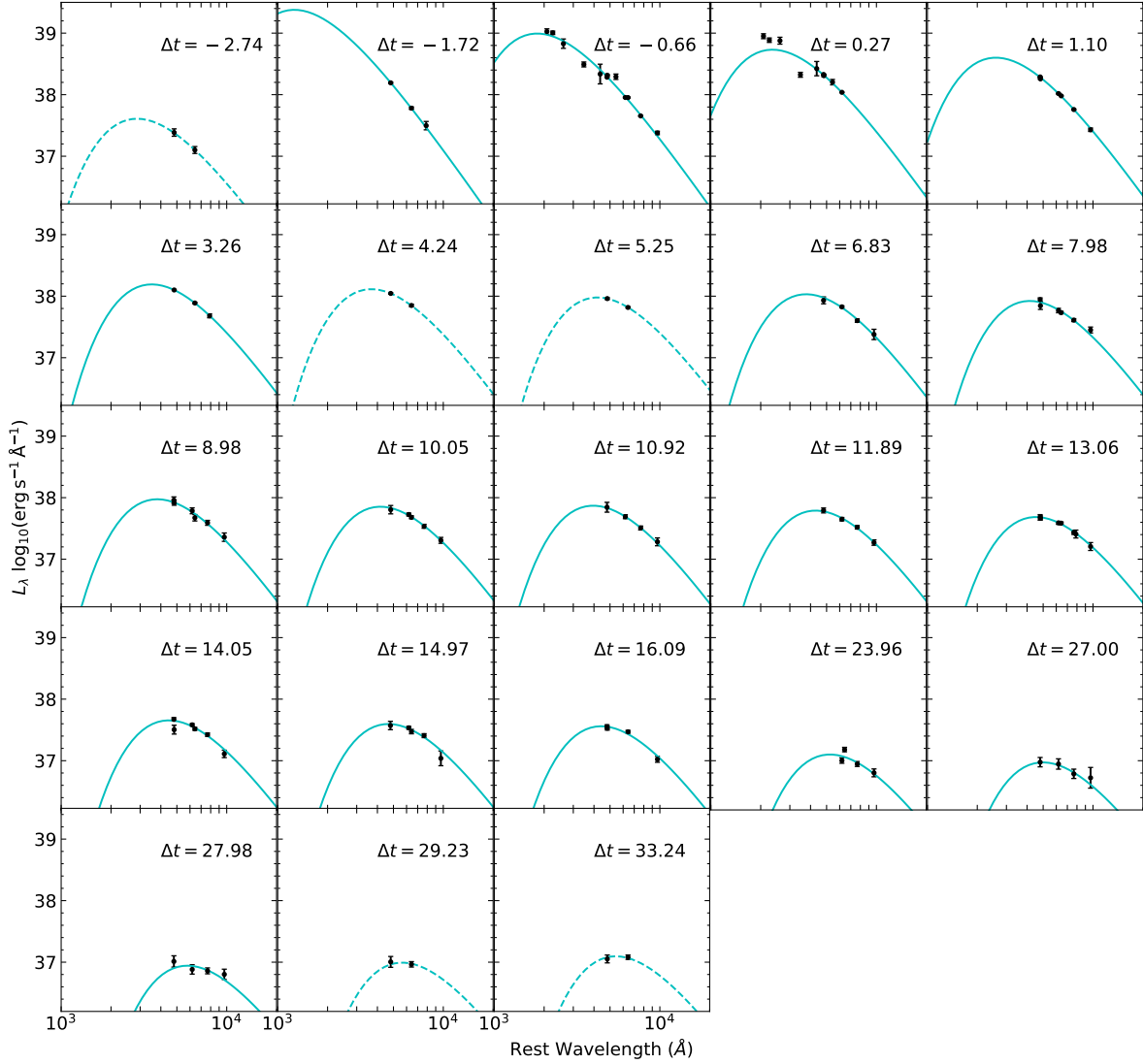
Figure A1. The maximum MCMC a posteriori model fits to $Swift$/UVOT and optical photometry for AT2019dge.

decay lifetimes of ^{56}Ni and ^{56}Co (Nadyozhin 1994). The effective heating rate is modified by the probability of thermalization, and thus $\varepsilon_{\text{heat}} \leq \varepsilon_{\text{rad}}$.

The bolometric light curve can be generally divided into the photospheric phase and the nebula phase. The photospheric phase can be modelled using Equations given in Valenti et al. (2008, Appendix A), with modifications given by Lyman et al. (2016, Eq. 3),

$$
\begin{aligned}
L_{\text{phot}}(t) = M_{\text{Ni}} e^{-x^2} \times \\
\left[(\epsilon_{\text{Ni}} - \epsilon_{\text{Co}}) \int_0^x (2z e^{-2zy + z^2}) \mathrm{d}z \right. \\
\left. + \epsilon_{\text{Co}} \int_0^x (2z e^{-2zy + 2zs + z^2}) \mathrm{d}z \right]
\end{aligned}
\tag{A4}
$$

where $x = t/\tau_{\text{m}}$, $y = \tau_{\text{m}}/(2\tau_{\text{Ni}})$,

$$
s = \frac{\tau_{\text{m}}(\tau_{\text{Co}} - \tau_{\text{Ni}})}{2\tau_{\text{Co}}\tau_{\text{Ni}}},
$$

$$
\tau_{\text{m}} = \left(\frac{2\kappa_{\text{opt}} M_{\text{ej}}}{13.8 c v_{\text{phot}}} \right)^{1/2}
\tag{A5}
$$

At the nebula phase the SN ejecta becomes optically thin, such that the delay between the energy deposition from radioactivity and the optical radiation becomes shorter. The bolometric luminosity is then equal to the rate of energy deposition: $L_{\text{neb}}(t) = Q(t)$. At any given time, the energy deposition rate $Q(t)$ is (Wheeler et al. 2015; Wygoda et al. 2019):

$$
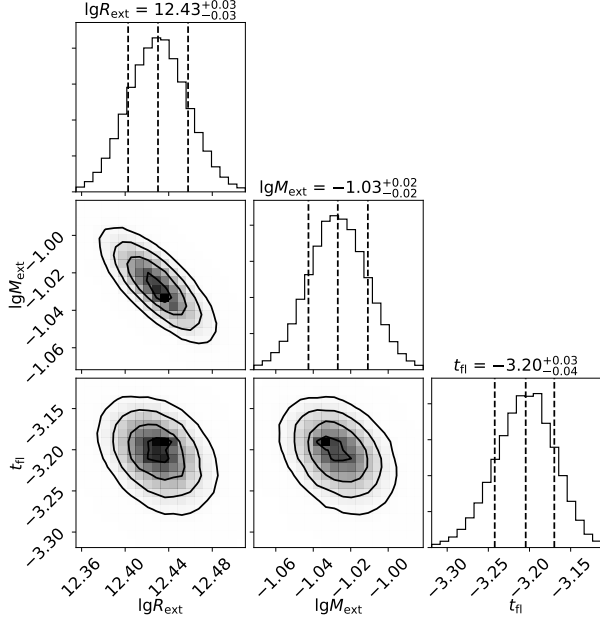Q(t) \approx Q_\gamma(t) \left(1 - e^{-(t_0/t)^2} \right)
\tag{A6}
$$

Figure A2. Corner plot showing the posterior constraints on $\lg R_{\rm ext}$, $\lg M_{\rm ext}$, and $t_{\rm fl}$. Marginalized one-dimensional distributions are shown along the diagonal, along with the median estimate and the 68% credible region (shown with vertical dashed lines).
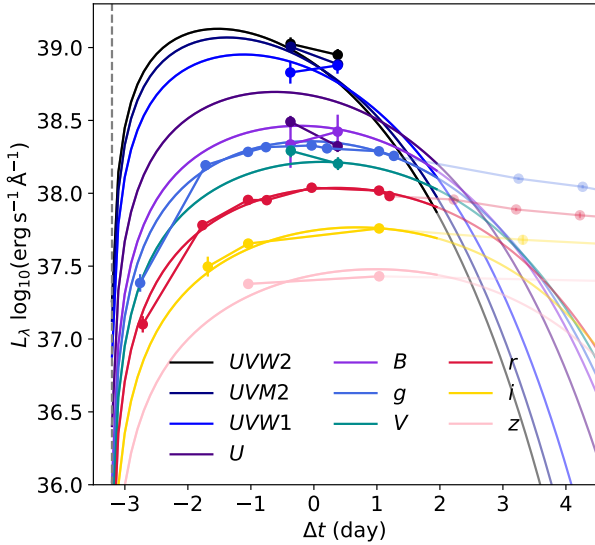
where $Q_\gamma(t) = M_{\rm Ni}\varepsilon_{\rm rad}$ is the energy release rate of gamma-rays, t_0 is the time at which the ejecta becomes optically thin to gamma rays. Here the difference between energy deposition rate of gamma-rays and positrons is neglected.

Table 6. ^{56}Ni decay model parameters θ and their priors

θ	Description	Prior
$\tau_{\rm m}$	characteristic photon diffusion time in day	$\mathcal{U}(1, 20)$
$\lg M_{\rm Ni}$	$\log_{10}$ of nickel mass in $M_\odot$	$\mathcal{U}(-4, 0)$
t_0	characteristic γ-ray escape time in day	$\mathcal{U}(1, 100)$

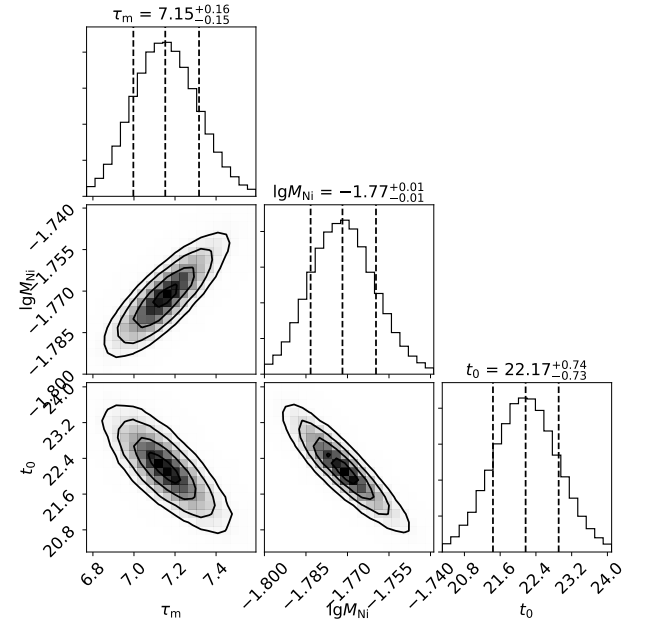**Figure A4.** Corner plot showing the posterior constraints on $\tau_{\rm m}$, $\lg M_{\rm Ni}$, and t_0. Marginalized one-dimensional distributions are shown along the diagonal, along with the median estimate and the 68% credible region (shown with vertical dashed lines).

Figure A3. Cooling emission model fit to the early light curve of AT2019dge. Data excluded from the fitting are shown as transparent circles. The maximum a posteriori model is shown via solid lines. The vertical dashed line shows the median 1-D marginalized posterior value of $t_{\rm fl}$.

To fit the shock cooling subtracted bolometric light curve with a simple radioactive decay model, we do not divide the data into photosperic phase and nebula phase, but instead adopt the following formula for the whole light curve:

$$L(t) = L_{\rm phot}(t)\left(1 - e^{-(t_0/t)^2}\right) \qquad (A7)$$

Priors or the model parameters are summarized in Table 6, and Figure A4 shows the coner plot of $\tau_{\rm m}$, $\lg M_{\rm Ni}$, and t_0.

Appendix B   UV and Optical Spectroscopy

B.1   Data

The log of UV and optical spectroscopy is presented in Table 7.

We use line centers of nebular lines to derive the spectroscopic redshift of the host (Table 8). The mean of all centroids gives $z = 0.0213 \pm 0.0001$.

B.2   Mass Loss Estimate from He II

Assuming that the CSM around the progenitor has a sperical wind-density profile of the form $\rho = Kr^{-2}$, where r is distance from the progenitor, $K \equiv \dot{M}/(4\pi v_{\rm w})$ is the mass loading parameter, $v_{\rm w}$ is the wind/outburst velocity, and $\dot{M}$ is the mass loss rate. The integrated mass of the emitting material from r to r_1 is

$$M_{\rm He} = \int_r^{r_1} 4\pi r^2 \rho(r) {\rm d}r \, 4\pi K(r_1 - r) = 4\pi K\beta r \quad \text{(B8)}$$

where $\beta \equiv (r_1 - r)/r$ is assumed to be of the order unity.

Following De et al. (2018a), we can relate the mass of the He II region to the He II $\lambda 4686$ line luminosity using

$$L_{\lambda 4686} \approx \frac{An_e M_{\rm He}}{m_{\rm He}}. \quad \text{(B9)}$$

Here

$$A = \frac{4\pi j_{\lambda 4686}}{n_e n_{\rm He^{++}}}, \quad \text{(B10)}$$

$j_{\lambda 4868}$ (in $\rm erg\,cm^{-3}\,s^{-1}\,sr^{-1}$) is the emission coefficient for the $\lambda 4686$ transition. $m_{\rm He}$ is mass of a He nucleus, $n_{\rm He^{++}}$ is the number density of doubly ionized helium and n_e is the number density of electrons.

Assuming a temperature of 10^4 K, electron density of 10^{10} cm^{-3}, and Case B recombination, we get $A = 1.32 \times 10^{-24}\,\rm erg\,cm^3\,s^{-1}$ (Storey & Hummer 1995). Assuming

$n_e = 2n_{\rm He^{++}}$ and using the density profile, Eq. (B9) can be written as

$$L_{\lambda 4686} \approx \frac{8\pi A\beta}{m_{\rm He}^2} \frac{K^2}{r}. \quad \text{(B11)}$$

The location of the emitting region can be constrained by requiring that the Thompson optical depth (τ) in the region must be small for the lines to escape. We require

$$\tau = n_e \sigma_{\rm T} \int_r^{r_1} {\rm d}r = 2n_{\rm He^{++}} \sigma_{\rm T} r\beta = \frac{2\sigma_{\rm T} r\beta}{m_{\rm He}} \frac{K}{r^2}$$
$$= \frac{2\sigma_{\rm T} K\beta}{m_{\rm He} r} \lesssim 1 \quad \text{(B12)}$$

Thus

$$r^2 \gtrsim \left(\frac{2\sigma_{\rm T}\beta}{m_{\rm He}}\right)^2 \frac{L_{\lambda 4686} m_{\rm He}^2 r}{8\pi A\beta}$$
$$r \gtrsim L_{\lambda 4686} \frac{\sigma_{\rm T}^2 \beta}{2\pi A} \quad \text{(B13)}$$

The $+0.4$ d emission line flux is meausred to be $F = (8.37 \pm 0.65) \times 10^{-16}\,\rm erg\,cm^{-2}\,s^{-1}$, correslonding to $L_{\lambda 4686} = 8.6 \times 10^{38}\,\rm erg\,s^{-1}$. Hence, we get $r \gtrsim 4.8 \times 10^{13}\beta$ cm, $K \gtrsim 1.2 \times 10^{14}\,\rm g\,cm^{-1}$, and $M_{\rm He} \gtrsim 3.6 \times 10^{-5}\beta^2\,M_\odot$.

Note that the above calculate only assumes that recombination is the primary line-emitting mechanism, and that collisional excitation and de-excitation processes can be ignored. to-do: rewrite this: the inferred radius ot optically thin material is larger than the envelope producing the early shock cooling emission as seen inthe light curve, and suggests that the highly ionized lines likely arise from a lower density extension of the same envelope?

to-do: Ask Kishalay: what is the light travel time blah blah argument – Now that the recombination timesclae is very short,

References

Alam, S., Albareti, F. D., Allende Prieto, C., et al. 2015, ApJS, 219, 12

Arcavi, I., Hosseinzadeh, G., Brown, P. J., et al. 2017, ApJL, 837, L2

Arnett, W. D. 1982, ApJ, 253, 785

Astropy Collaboration, Robitaille, T. P., Tollerud, E. J., et al. 2013, A&A, 558, A33

Bellm, E. C., & Sesar, B. 2016, pyraf-dbsp: Reduction pipeline for the Palomar Double Beam Spectrograph

Bellm, E. C., Kulkarni, S. R., Graham, M. J., et al. 2019a, PASP, 131, 018002

Bellm, E. C., Kulkarni, S. R., Barlow, T., et al. 2019b, PASP, 131, 068003

Boquien, M., Burgarella, D., Roehlly, Y., et al. 2019, A&A, 622, A103

Bruzual, G., & Charlot, S. 2003, MNRAS, 344, 1000

Bufano, F., Immler, S., Turatto, M., et al. 2009, ApJ, 700, 1456

Calzetti, D., Armus, L., Bohlin, R. C., et al. 2000, ApJ, 533, 682

Cardelli, J. A., Clayton, G. C., & Mathis, J. S. 1989, ApJ, 345, 245

Chabrier, G. 2003, PASP, 115, 763

Chen, P., Dong, S., Stritzinger, M. D., et al. 2020, ApJL, 889, L6

Chevalier, R. A., & Irwin, C. M. 2011, ApJL, 729, L6

Table 7. Log of AT2019dge spectroscopy.

Start Time (UTC)	Instrument	Δt (day)	Exposure Time	Airmass (s)	Resolution (FWHM Å)
2019 Apr 09 03:30:28	LT+SPART	-1.1	500	1.800	18
2019 Apr 10 03:06:10	LT+SPART	-0.1	500	1.800	18
2019 Apr 10 14:21:44	Keck1+LRIS	$+0.4$	300	1.169	6
2019 Apr 12 05:08:00	HST+WFC3+UVIS	$+12.0$	2×250	—	43
2019 Apr 24 11:06:43	P200+DBSP	$+14.3$	1200	1.047	3–5
2019 Jul 04 11:49:18	Keck1+LRIS	$+85.3$	1740	1.421	6
2019 Aug 31 08:04:58	Keck1+LRIS	$+143.1$	1150	1.409	6
2019 Sep 28 08:14:27	Keck1+LRIS	$+171.1$	600	2.165	6
2020 Feb 18 15:23:40	Keck1+LRIS	$+314.4$	1450	1.384	6

Table 8. Line fluxes from the host galaxy of AT2019dge extracted from the Keck/LRIS spectrum obtained on Aug xx 2019.

Transition	λ_{obs} (Å)	F $(10^{-16}\ \mathrm{erg\,cm^{-2}\,s^{-1}})$
Hβ	4862.35 ± 0.21	32.45 ± 2.08
[O III]λ5007	5007.06 ± 0.55	67.56 ± 13.52
Hα	6562.07 ± 0.03	115.79 ± 1.16
[N II]λ6583	6582.62 ± 0.08	8.89 ± 0.37

Note—All measurements are corrected for Galactic reddening.

Table 9. Photometry of the host galaxy

Instrument/ Filter	λ_{eff} (Å)	Brightness (mag)
SDSS/u'	3594.9	19.336 ± 0.039
SDSS/g'	4640.4	18.322 ± 0.009
SDSS/r'	6122.3	17.913 ± 0.009
SDSS/i'	7439.5	17.745 ± 0.010
SDSS/z'	8897.1	17.580 ± 0.031
WISE/$W1$	33526.0	15.938 ± 0.037
WISE/$W2$	46028.0	15.982 ± 0.082

Note—SDSS (Alam et al. 2015) measurements are reported in the AB system. AllWISE (Cutri & et al. 2013) measurements are in the Vega system and the conversion to flux density are performed using Jarrett et al. (2011, Table 1). Values are not corrected for reddening.

Chornock, R., Filippenko, A. V., Li, W., et al. 2011, ApJ, 739, 41

Cutri, R. M., & et al. 2013, VizieR Online Data Catalog, II/328

De, K., Kasliwal, M. M., Ofek, E. O., et al. 2018a, Science, 362, 201

De, K., Kasliwal, M. M., Cantwell, T., et al. 2018b, ApJ, 866, 72

Dey, A., Schlegel, D. J., Lang, D., et al. 2019, AJ, 157, 168

Draine, B. T., & Li, A. 2007, ApJ, 657, 810

Drout, M. R., Soderberg, A. M., Gal-Yam, A., et al. 2011, ApJ, 741, 97

Drout, M. R., Soderberg, A. M., Mazzali, P. A., et al. 2013, ApJ, 774, 58

Folatelli, G., Contreras, C., Phillips, M. M., et al. 2006, ApJ, 641, 1039

Foreman-Mackey, D. 2016, JOSS, 24

Foreman-Mackey, D., Hogg, D. W., Lang, D., & Goodman, J. 2013, Publications of the Astronomical Society of the Pacific, 125, 306

Fremling, C., Sollerman, J., Taddia, F., et al. 2016, A&A, 593, A68

Fremling, C., Ko, H., Dugas, A., et al. 2019, ApJL, 878, L5

Gal-Yam, A., Bufano, F., Barlow, T. A., et al. 2008, ApJL, 685, L117

Galbany, L., Ashall, C., Hoeflich, P., et al. 2019, arXiv, arXiv:1904.10034

Gehrels, N., Chincarini, G., Giommi, P., et al. 2004, ApJ, 611, 1005

Graham, M. J., Kulkarni, S. R., Bellm, E. C., et al. 2019, arXiv

Guillochon, J., Parrent, J., Kelley, L. Z., & Margutti, R. 2017, ApJ, 835, 64

Ho, A. Y. Q., Goldstein, D. A., Schulze, S., et al. 2019, ApJ, 887, 169

Ho, P. T. P., Moran, J. M., & Lo, K. Y. 2004, ApJL, 616, L1

Hotokezaka, K., Kashiyama, K., & Murase, K. 2017, ApJ, 850, 18

Hunter, J. D. 2007, Computing In Science & Engineering, 9, 90

Inserra, C., Sim, S. A., Wyrzykowski, L., et al. 2015, ApJL, 799, L2

Jacobson-Galan, W. V., Polin, A., Foley, R. J., et al. 2019, arXiv, arXiv:1910.05436

Jarrett, T. H., Cohen, M., Masci, F., et al. 2011, ApJ, 735, 112

Jeffery, D. J., Kirshner, R. P., Challis, P. M., et al. 1994, ApJL, 421, L27

Jones, E., Oliphant, T., Peterson, P., et al. 2001–, SciPy: Open source scientific tools for Python

Kasen, D. 2017, Unusual Supernovae and Alternative Power Sources, ed. A. W. Alsabti & P. Murdin, 939

Kasliwal, M. M., Kulkarni, S. R., Gal-Yam, A., et al. 2010, ApJL, 723, L98

—. 2012, ApJ, 755, 161

Kasliwal, M. M., Cannella, C., Bagdasaryan, A., et al. 2019, PASP, 131, 038003

Kennicutt, Robert C., J. 1998, ApJ, 498, 541

Khatami, D. K., & Kasen, D. N. 2019, ApJ, 878, 56

Khazov, D., Yaron, O., Gal-Yam, A., et al. 2016, ApJ, 818, 3

Kleiser, I., Fuller, J., & Kasen, D. 2018, MNRAS, 481, L141

Komatsu, E., Smith, K. M., Dunkley, J., et al. 2011, ApJS, 192, 18

Leonard, D. C., Filippenko, A. V., Barth, A. J., & Matheson, T. 2000, ApJ, 536, 239

Luridiana, V., Morisset, C., & Shaw, R. A. 2013, PyNeb: Analysis of emission lines

Lyman, J. D., Bersier, D., James, P. A., et al. 2016, MNRAS, 457, 328

Madau, P., & Dickinson, M. 2014, ARA&A, 52, 415

Mahabal, A., Rebbapragada, U., Walters, R., et al. 2019, PASP, 131, 038002

Margalit, B., & Metzger, B. D. 2016, MNRAS, 461, 1154

Marino, R. A., Rosales-Ortega, F. F., Sánchez, S. F., et al. 2013, A&A, 559, A114

Mazzali, P. A., Sullivan, M., Hachinger, S., et al. 2014, MNRAS, 439, 1959

McBrien, O. R., Smartt, S. J., Chen, T.-W., et al. 2019, ApJL, 885, L23

McKinney, W. 2010, 51

Metzger, B. D., Piro, A. L., & Quataert, E. 2009, MNRAS, 396, 1659

Modjaz, M., Gutiérrez, C. P., & Arcavi, I. 2019, NatAs, 3, 717

Moriya, T., Tominaga, N., Tanaka, M., et al. 2010, ApJ, 719, 1445

Nadyozhin, D. K. 1994, ApJS, 92, 527

Nakar, E., & Piro, A. L. 2014, ApJ, 788, 193

Ofek, E. O., Lin, L., Kouveliotou, C., et al. 2013, ApJ, 768, 47

Oke, J. B., & Gunn, J. E. 1982, PASP, 94, 586

Oke, J. B., Cohen, J. G., Carr, M., et al. 1995, PASP, 107, 375

Patterson, M. T., Bellm, E. C., Rusholme, B., et al. 2019, PASP, 131, 018001

Perley, D. A. 2019, PASP, 131, 084503

Pettini, M., & Pagel, B. E. J. 2004, MNRAS, 348, L59

Piascik, A. S., Steele, I. A., Bates, S. D., et al. 2014, Society of Photo-Optical Instrumentation Engineers (SPIE) Conference Series, Vol. 9147, SPRAT: Spectrograph for the Rapid Acquisition of Transients, 91478H

Piro, A. L. 2015, ApJL, 808, L51

Poznanski, D., Chornock, R., Nugent, P. E., et al. 2010, Science, 327, 58

Prentice, S. J., Ashall, C., James, P. A., et al. 2019, MNRAS, 485, 1559

Rest, A., Garnavich, P. M., Khatami, D., et al. 2018, NatAs, 2, 307

Roming, P. W. A., Kennedy, T. E., Mason, K. O., et al. 2005, SSRv, 120, 95

Schlafly, E. F., & Finkbeiner, D. P. 2011, ApJ, 737, 103

Schlegel, D. J., Finkbeiner, D. P., & Davis, M. 1998, ApJ, 500, 525

Shen, K. J., Kasen, D., Weinberg, N. N., et al. 2010, ApJ, 715, 767

Shiode, J. H., & Quataert, E. 2014, ApJ, 780, 96

Sim, S. A., Fink, M., Kromer, M., et al. 2012, MNRAS, 420, 3003

Steele, I. A., Smith, R. J., Rees, P. C., et al. 2004, Proc. SPIE, 5489, 679

Storey, P. J., & Hummer, D. G. 1995, MNRAS, 272, 41

Sullivan, M., Kasliwal, M. M., Nugent, P. E., et al. 2011, ApJ, 732, 118

Tauris, T. M., Langer, N., & Podsiadlowski, P. 2015, MNRAS, 451, 2123

Valenti, S., Benetti, S., Cappellaro, E., et al. 2008, MNRAS, 383, 1485

Wheeler, J. C., Johnson, V., & Clocchiatti, A. 2015, MNRAS, 450, 1295

Whitesides, L., Lunnan, R., Kasliwal, M. M., et al. 2017, ApJ, 851, 107

Woosley, S. E. 2019, ApJ, 878, 49

Wygoda, N., Elbaz, Y., & Katz, B. 2019, MNRAS, 484, 3951

Yan, L., Quimby, R., Gal-Yam, A., et al. 2017, ApJ, 840, 57

Yao, Y., Miller, A. A., Kulkarni, S. R., et al. 2019, ApJ, 886, 152

Yaron, O., & Gal-Yam, A. 2012, PASP, 124, 668

Zou, H., Zhang, T., Zhou, Z., et al. 2017, AJ, 153, 276